J. Fluid Mech. (2024), *vol*. 988, A14, doi:10.1017/jfm.2024.381

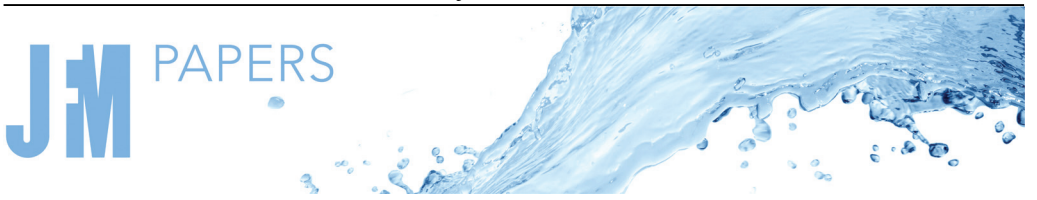

Fluctuation covariance-based study of roll-streak dynamics in Poiseuille flow turbulence

Marios-Andreas Nikolaidis[1], **Petros J. Ioannou**[1,2,†] **and Brian F. Farrell**[2]

[1]Department of Physics, National and Kapodistrian University of Athens, Athens 15784, Greece

[2]Department of Earth and Planetary Sciences, Harvard University, Cambridge, MA 02138, USA

(Received 5 September 2023; revised 14 March 2024; accepted 1 April 2024)

Although the roll-streak (R-S) is fundamentally involved in the dynamics of wall turbulence, the physical mechanism responsible for its formation and maintenance remains controversial. In this work we investigate the dynamics maintaining the R-S in turbulent Poiseuille flow at $R = 1650$. Spanwise collocation is used to remove spanwise displacement of the streaks and associated flow components, which isolates the streamwise-mean flow R-S component and the second-order statistics of the streamwise-varying fluctuations that are collocated with the R-S. This partition of the dynamics into streamwise-mean and fluctuation components facilitates exploiting insights gained from the analytic characterization of turbulence in the second-order statistical state dynamics (SSD), referred to as S3T, and its closely associated restricted nonlinear dynamics (RNL) approximation. Symmetry of the statistics about the streak centreline permits separation of the fluctuations into sinuous and varicose components. The Reynolds stress forcing induced by the sinuous and varicose fluctuations acting on the R-S is shown to reinforce low- and high-speed streaks, respectively. This targeted reinforcement of streaks by the Reynolds stresses occurs continuously as the fluctuation field is strained by the streamwise-mean streak and not intermittently as would be associated with streak-breakdown events. The Reynolds stresses maintaining the streamwise-mean roll arise primarily from the dominant proper orthogonal decomposition (POD) modes of the fluctuations, which can be identified with the time average structure of optimal perturbations growing on the streak. These results are consistent with a universal process of R-S growth and maintenance in turbulent shear flow arising from roll forcing generated by straining turbulent fluctuations, which was identified using the S3T SSD.

Key words: pattern formation, pipe flow

† Email address for correspondence: pjioannou@phys.uoa.gr

1. Introduction

Although turbulent flows exhibit fluctuations indicative of a stochastic process, closer analysis reveals elements of underlying order. Efforts to identify and analyse the origin of this underlying order in turbulence led to the introduction of a structure measure, the two-point correlation function, which was originally interpreted to provide an influence distance from measurements of flow velocities (Taylor 1935). Progress in measuring apparatus subsequently allowed the collection of increasingly resolved data sets and Lumley (1967) proposed a method to identify coherent structures arising in turbulent flows making use of two-point spatial correlation in the flow. In tandem with identification of coherent structure arising from advances in experimental observations were attempts to provide a theoretical basis for the emergence of these coherent structures, a summary of which can be found in the reviews by Cantwell (1981), Robinson (1991) and Jiménez (2018). Advances in flow visualization provided additional evidence of coherent structure in turbulent shear flows not only in the buffer layer but including organized large-scale and very large-scale motions throughout turbulent shear flows e.g. (Hutchins & Marusic 2007; Hellström, Sinha & Smits 2011).

A prominent component of the coherent structure observed in turbulent shear flow is the roll-streak (R-S) structure. This coherent structure alone accounts for a significant fraction of the turbulent fluctuation kinetic energy and considerable effort has been devoted to identifying the mechanisms forming and maintaining the R-S (Benney 1960; Jang, Benney & Gran 1986; Hall & Smith 1991; Hamilton, Kim & Waleffe 1995; Waleffe 1997; Schoppa & Hussain 2002; Flores & Jiménez 2010; Hall & Sherwin 2010; Hwang & Cossu 2010, 2011; Farrell & Ioannou 2012; Rawat *et al.* 2015; Cossu & Hwang 2017; Kwon & Jiménez 2021). As a result of these efforts, it became apparent that the R-S is an important component of not only the energy bearing structures but also of the dynamics underlying the maintenance of wall turbulence. One role of the R-S in supporting turbulence is to transfer streamwise mean momentum from the spanwise homogeneous equilibrium flow, which is maintained by external mean pressure or boundary-associated forcing, to form a spanwise inhomogeneous streak in the flow by the lift-up process (Ellingsen & Palm 1975; Landahl 1980). This streak in turn makes available rapidly growing streamwise and spanwise dependent perturbations that support subsequent energy transfers from the streamwise-mean flow to the fluctuation field required to both generate and maintain the turbulent state. An example of the former being transition to turbulence (Westin *et al.* 1994; Brandt, Schlatter & Henningson 2004) and of the latter the self-sustaining process (SSP) mechanism (Hamilton *et al.* 1995; Waleffe 1997).

The fact that the R-S does not arise as a modal instability when the Navier–Stokes equations (NSE) expressed in velocity variables are linearized about the streamwise-mean flow led to the belief that the R-S does not arise as an unstable mode in the NSE. Nonetheless, in shear flow the R-S is the optimally growing structure in the NSE expressed in velocity state variables. This has been studied in both the time domain (Butler & Farrell 1992; Reddy & Henningson 1993) and frequency domain (McKeon & Sharma 2010; McKeon 2017), so that the occurrence of optimals with R-S form arising from transient growth of fluctuations in the turbulence provides a plausible explanation for the common observation of this structure in turbulent shear flows. However, R-S formation through transient growth produces initial algebraic growth followed by decay in time and, if randomly forced, a stochastic distribution in space because transient growth lacks an organizational mechanism that would produce temporal persistence and spatial organization of the R-S. The ubiquity, persistence and large scale organization of the

R-S in turbulent shear flow despite lack of a modal R-S formation instability in the traditional NSE formulation resulted in attempts to uncover explanations alternative to transient growth of initial or continuously forced perturbations to explain the formation and maintenance of the R-S. Among these mechanisms are various regeneration or self-sustaining processes (Jiménez & Moin 1991; Hamilton *et al.* 1995; Waleffe 1997; Jiménez & Pinelli 1999; Schoppa & Hussain 2002; Hall & Sherwin 2010; Deguchi & Hall 2016). Alternatively, the R-S has been attributed to unstable exact coherent structures (ECS) (Waleffe 2001; Halcrow *et al.* 2009). While unstable ECS can resemble R-Ss, the R-Ss in this study, as well as the preponderance of those in Poiseuille flow turbulence, are hydrodynamically stable (Schoppa & Hussain 2002) rather than unstable, as are the ECSs.

It is now recognized that the R-S can arise from a modal instability when the NSE are expressed in cumulant variables and linearized about the streamwise-mean flow associated with a background of turbulent fluctuations. This modal instability had been overlooked because it has analytic expression only when the NSE are written using a statistical state dynamics (SSD) formulation, such as the second order SSD referred to as S3T (Farrell & Ioannou 2012; Farrell, Ioannou & Nikolaidis 2017*b*). The dynamics of the S3T SSD is closely approximated by the restricted nonlinear dynamics (RNL) equations, which allows insights from the essentially complete characterization of the analytical structure of wall turbulence dynamics by S3T to be transferred to RNL, and from RNL to its direct numerical simulation (DNS) companion (Thomas *et al.* 2014; Farrell *et al.* 2016; Farrell, Gayme & Ioannou 2017*a*). The crucial choice of dynamical significance in the formulation of both the S3T and its RNL approximation is to use a partition into streamwise-mean and fluctuations from the streamwise-mean. This particular partition is crucial to gaining insight into turbulence dynamics because it isolates the interaction between these two components, which comprises the fundamental dynamics maintaining and regulating the turbulent state. The success of this partition in maintaining a realistic turbulent state when the associated SSD is closed at second order implies that interaction between the streamwise-mean flow and the covariance of fluctuations from the streamwise-mean suffices for understanding the physical mechanism sustaining and regulating turbulence in shear flow. Analysis of the S3T SSD reveals that the influence of the fluctuations on the streamwise mean component occurs through the fluctuation Reynolds stresses, which can be obtained from the covariance component of the SSD.

In agreement with simulations, R-S formation through the S3T modal instability produces initial exponential growth in time leading through nonlinear equilibration to persistent stable equilibrium R-S with coherent harmonic organization in space (Farrell *et al.* 2017*b*). Although in turbulent Poiseuille flow the R-S is subject to disruption, the organization mechanism inherent in the S3T dynamics still results in streamwise extended R-S in Poiseuille flow turbulence, while accounting for the observed persistence and harmonic organization of the R-S in the less disrupted wide channel Couette turbulence (Avsarkisov *et al.* 2014; Pirozzoli, Bernardini & Orlandi 2014; Lee & Moser 2018).

In this work we build on previous work in which the structure of the mean and fluctuation components of the R-S were identified using proper orthogonal decomposition (POD)-based methods (Nikolaidis *et al.* 2023). However, our aim in this work is to address not structure but rather dynamics; specifically, we analyse data obtained from DNS and RNL simulations of turbulent Poiseuille flows at $R = 1650$ concentrating on diagnosing the dynamical processes responsible for sustaining the R-S. In our study

of structure in Nikolaidis *et al.* (2023) we departed from traditional POD analysis by incorporating into the analysis the recognition that while the streamwise-mean R-S is an emergent coherent structure supported by the Reynolds-stresses of the streamwise-varying fluctuations, in turbulence this structure is subject to stochastic displacements in the homogeneous spanwise direction. In order to isolate the R-S structure, while refining the convergence of the second-order statistical quantities supporting it, we collocate the spanwise position of the R-S as indicated by the spanwise position of the spanwise varying streak. This method is similar in intent to the slicing and centring methods employed by Rowley & Marsden (2000), Froehlich & Cvitanović (2012), Willis, Cvitanović & Avila (2013), Kreilos, Zammert & Eckhardt (2014) and the conditional space–time (POD) method (Schmidt & Schmid 2019) used recently to obtain small-scale structure in turbulent boundary layers (Saxton-Fox, Lozano-Durán & McKeon 2022) and also to the method applied recently in dynamical mode decomposition in turbulent Couette and Poiseuille flows (Marensi *et al.* 2023). Using collocation we obtained in Nikolaidis *et al.* (2023) the mean structure of the low-speed and high-speed R-S and verified that these collocated R-S structures are nearly identical in DNS and RNL and that the associated fluctuations and Reynolds stresses are also compellingly similar. The mean streak was found to be perturbation stable in the NSE when the NSE are expressed in standard velocity variables and to be mirror-symmetric about the centreline in the spanwise direction. This mirror symmetry allows separation of the fluctuations about the centreline into linearly statistically independent odd and even components. The fluctuations with symmetric streamwise and wall-normal velocity components and antisymmetric spanwise velocity component are referred to as sinuous fluctuations ($\mathcal{S}$), while the fluctuations with antisymmetric streamwise and wall-normal velocity components and symmetric spanwise velocity component are referred to as varicose fluctuations ($\mathcal{V}$). While both $\mathcal{S}$ and $\mathcal{V}$ fluctuations are represented in the POD modes of both low- and high-speed streaks, the dominant POD modes of the fluctuations associated with the low-speed streak in both DNS and RNL comprise $\mathcal{S}$ oblique waves collocated with the streak. Moreover, these dominant fluctuation POD modes have the average structure of white-in-energy perturbations evolved linearly on the R-S, white-in-energy perturbations being chosen so that the perturbations that dominate the response reflect only the intrinsic dynamics of the evolution of the perturbations, which is determined by the perturbations with optimal growth. This result that the dominant POD modes of the streak excited white-in-energy have the same structure as the fluctuation POD modes in both DNS and RNL has a compelling interpretation: the background turbulence is being strained by the streak to produce the structures required to support that streak via the SSP mechanism and these structures can be identified with the optimal perturbations on the streak (Nikolaidis *et al.* 2023).

Having identified and characterized the mean low-speed and high-speed streaks and the streak-collocated fluctuation fields, we proceed in this report to study the streamwise-mean Reynolds stresses arising from these fluctuations in order to identify the dynamical mechanism responsible for sustaining the rolls that give rise through lift-up to the streaks in both DNS and RNL. A motivation for establishing the correspondence in the physical mechanism of the SSP between DNS and RNL is that RNL shares its dynamical structure with S3T so that establishing correspondence of the SSP in DNS and RNL implies that the SSP structure and mechanism in DNS is dynamically the same as that in S3T, which is completely characterized, and therefore establishing this correspondence is tantamount to achieving an analytic characterization of the SSP underlying wall turbulence in the DNS.

2. Model problem and numerical methods

The data is obtained from a DNS of a pressure-driven constant mass flux plane Poiseuille flow in a channel which is doubly periodic in the streamwise, x, and spanwise, z, directions. The velocity field is decomposed into the streamwise-mean component $\boldsymbol{U} = (U, V, W)$ and fluctuations from the mean, $\boldsymbol{u} = (u, v, w)$. In this decomposition the R-S is part of the mean component of the flow with the streak component defined as $U_s(y, z, t) = U - [U]$, where the square brackets $[\cdot] \stackrel{\text{def}}{=} (1/L_z)\int_0^{L_z} \cdot \, \mathrm{d}z$ denote the spanwise average, and the roll component has velocities components $(0, V, W)$.

The incompressible non-dimensional NSE governing the channel flow in this decomposition are

$$\partial_t \boldsymbol{U} + \boldsymbol{U}\cdot\boldsymbol{\nabla}\boldsymbol{U} - \Pi(t)\hat{\boldsymbol{x}} + \boldsymbol{\nabla}P - R^{-1}\Delta\boldsymbol{U} = -\overline{\boldsymbol{u}\cdot\boldsymbol{\nabla}\boldsymbol{u}}, \tag{2.1a}$$

$$\partial_t \boldsymbol{u} + \boldsymbol{U}\cdot\boldsymbol{\nabla}\boldsymbol{u} + \boldsymbol{u}\cdot\boldsymbol{\nabla}\boldsymbol{U} + \boldsymbol{\nabla}p - R^{-1}\Delta\boldsymbol{u} = -(\boldsymbol{u}\cdot\boldsymbol{\nabla}\boldsymbol{u} - \overline{\boldsymbol{u}\cdot\boldsymbol{\nabla}\boldsymbol{u}}), \tag{2.1b}$$

$$\boldsymbol{\nabla}\cdot\boldsymbol{U} = 0, \quad \boldsymbol{\nabla}\cdot\boldsymbol{u} = 0. \tag{2.1c}$$

The pressure gradient $\Pi(t)$ is adjusted in time to maintain constant mass flux. Lengths have been made non-dimensional by h, the channel's half-width, velocities by the time-mean velocity at the centre of the channel, U_c, and time by h/U_c. Averaging in x is denoted by $\overline{(\cdot)}$ and averaging in time by $\langle\cdot\rangle$. No-slip and impermeable boundaries are placed at $y = 0$ and $y = 2$, in the wall-normal variable. The Reynolds number is $R = U_c h/\nu$, with ν the kinematic viscosity.

The DNS is obtained using NSE (2.1) and for comparison, parallel simulations are made with the RNL approximation of (2.1), which is obtained by parameterizing the fluctuation–fluctuation nonlinearity in (2.1*b*). The parameterization used is to set these nonlinear interactions among streamwise non-constant flow components in the fluctuation equations (2.1*b*) to zero. Consequently, the RNL system of equations is

$$\partial_t \boldsymbol{U} + \boldsymbol{U}\cdot\boldsymbol{\nabla}\boldsymbol{U} - \Pi(t)\hat{\boldsymbol{x}} + \boldsymbol{\nabla}P - R^{-1}\Delta\boldsymbol{U} = -\overline{\boldsymbol{u}\cdot\boldsymbol{\nabla}\boldsymbol{u}}, \tag{2.2a}$$

$$\partial_t \boldsymbol{u} + \boldsymbol{U}\cdot\boldsymbol{\nabla}\boldsymbol{u} + \boldsymbol{u}\cdot\boldsymbol{\nabla}\boldsymbol{U} + \boldsymbol{\nabla}p - R^{-1}\Delta\boldsymbol{u} = 0. \tag{2.2b}$$

$$\boldsymbol{\nabla}\cdot\boldsymbol{U} = 0, \quad \boldsymbol{\nabla}\cdot\boldsymbol{u} = 0. \tag{2.2c}$$

Under this quasilinear restriction, the fluctuation field interacts nonlinearly only with the mean, $\boldsymbol{U}$, flow and not with itself. This quasilinear restriction of the dynamics results in the spontaneous collapse in the support of the fluctuation field to a small subset of streamwise Fourier components, while maintaining conservation of the total flow energy $1/2\int_{\mathcal{D}} d^3\boldsymbol{x}(|\boldsymbol{U}|^2 + |\boldsymbol{u}|^2)$ in the absence of dissipation ($\mathcal{D}$ is the flow domain). This restriction in the support of RNL turbulence to a small subset of streamwise Fourier components is not imposed but rather is a property of the quasilinear dynamics. The fluctuation components retained by the dynamics identify the streamwise harmonics that are energetically active in the parametric growth process that sustains the fluctuations (Farrell & Ioannou 2012; Constantinou, Farrell & Ioannou 2014; Thomas *et al.* 2014, 2015; Farrell *et al.* 2016). In a DNS at $R = 2250$ these energetically active streamwise harmonics have been shown to synchronize the remaining components (Nikolaidis & Ioannou 2022).

The data were obtained from a DNS of (2.1), referred to as NSE100, and from the associated RNL governed by (2.2), referred to as RNL100. The Reynolds number $R = U_c h/\nu = 1650$ is imposed in both the DNS and the RNL simulations. A summary of the parameters of the simulations is given in table 1. The RNL100 simulation is supported

Abbreviation	$[L_x, L_z]/h$	$[\alpha, \beta]$	$N_x \times N_z \times N_y$	R_τ	R
NSE100	$[4\pi, \pi]$	[0.5,2]	$128 \times 63 \times 97$	100.59	1650
RNL100	$[4\pi, \pi]$	[0.5,2]	$16 \times 63 \times 97$	93.18	1650

Table 1. Simulation parameters: $[L_x, L_z]/h$ is the domain size in the streamwise, spanwise direction; $[\alpha, \beta] = [2\pi/L_x, 2\pi/L_z]$ denote the fundamental wavenumbers in the streamwise and spanwise directions; N_x, N_z are the number of Fourier components after dealiasing and N_y is the number of Chebyshev components; $R_\tau = u_\tau h/\nu$ is the Reynolds number of the simulation based on the friction velocity $u_\tau = \sqrt{\nu\, \mathrm{d}[U]/\mathrm{d}y|_w}$, where $\mathrm{d}[U]/\mathrm{d}y|_w$ is the shear at the wall.

by only three streamwise components with wavelengths $\lambda_x/h = 4\pi, 2\pi, 4\pi/3$, which correspond to the three lowest streamwise Fourier components of the channel, $n_x = 1, 2, 3$.

For the numerical integration the dynamics were expressed in the form of evolution equations for the wall-normal vorticity and the Laplacian of the wall-normal velocity, with spatial discretization and Fourier dealiasing in the two wall-parallel directions and Chebychev polynomials in the wall-normal direction (Kim, Moin & Moser 1987). Time stepping was implemented using the third-order semi-implicit Runge–Kutta method.

3. Obtaining the streamwise-mean R-S and the covariance of the associated fluctuations using collocation

In order to analyse the dynamics of the R-S we obtain both the streamwise-mean R-S and the time-mean spatial two-point covariances of the fluctuations collocated with the R-S for both the high-speed and the low-speed streak. The collocation implementation is described in Nikolaidis *et al.* (2023). Briefly the method proceeds by identifying the spanwise location of the streak with the location of the spanwise coordinate of the $\min(U_s)$ (for low-speed streaks) and translating the entire flow field in the spanwise direction to place the low-speed streak minimum at the channel centre $z/h = 0$. We have verified that as the averaging time increases the time-mean streak approaches mirror symmetry in the spanwise about the streak centreline. We enforce this symmetry in the dataset and double the available data by symmetrizing about the aligned streak centre.

The time-mean streak, $\langle U_s \rangle$, obtained from the aligned time series of $\min(U_s)$ isolates the low-speed streak, producing a coherent low-speed R-S at $z/h = 0$, while away from this core region the velocity components cancel indicative of their being incoherently correlated with the centred streak. This collocation procedure is similarly implemented to isolate the high-speed streak. The structures in the y–z plane of the time-mean low-speed and high-speed R-S in NSE100 are shown in figure 1(*a*,*b*) using contours for $\langle U_s \rangle$ and vectors for $(\langle W \rangle, \langle V \rangle)$. The time-mean flow in the upper region, $y/h > 1$, is to a good approximation spanwise homogeneous (not shown). The structure of the time-mean streaks in RNL100 are similar (cf. Nikolaidis *et al.* 2023). It is important to note that although low-speed streaks are associated with flanking high-speed streak components, the low-speed streaks are isolated structures in the statistical mean because of the decoherence of the spanwise location of the streaks in Poiseuille flow. In contrast, simulations of Couette flow turbulence in wide channels reveal that the streaks exhibit long range correlation (Avsarkisov *et al.* 2014; Pirozzoli *et al.* 2014; Lee & Moser 2018). The implication is that in wide channel Couette flow a collocation procedure would not be necessary because the turbulence would exhibit a full array of spanwise periodic low- and high-speed R-S rather than the random distribution of isolated R-S seen in Poiseuille flow.

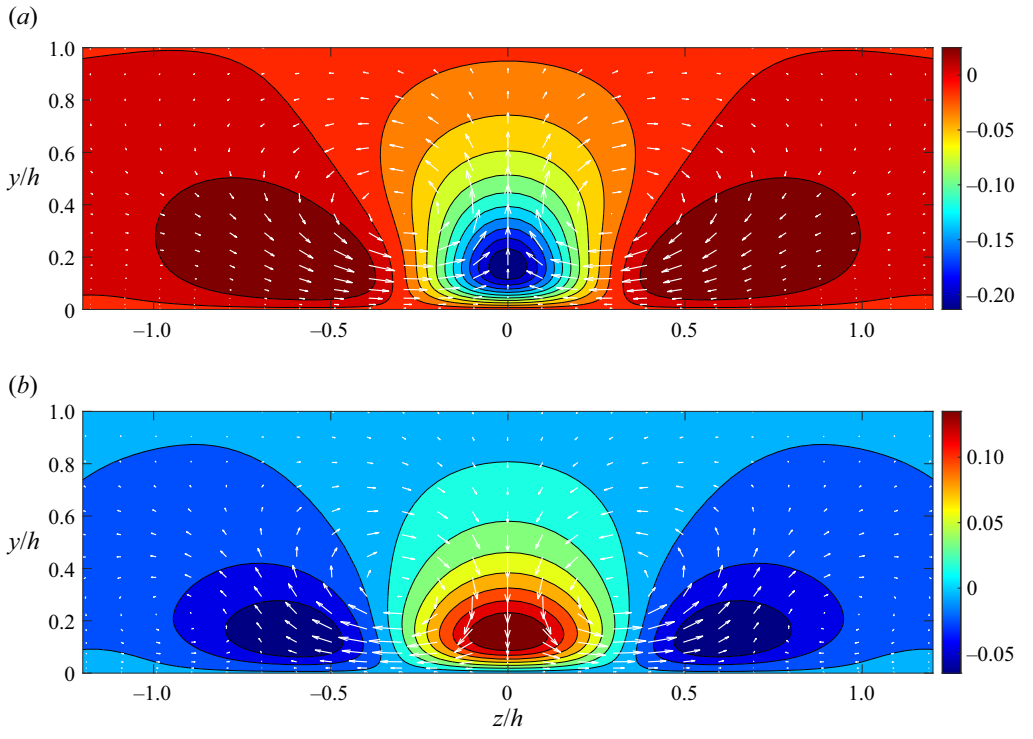

Figure 1. Contours of the time-mean collocated streak, $\langle U_s \rangle$, and vectors of the roll velocity, $(\langle W \rangle, \langle V \rangle)$, for the NSE100 low-speed streak (*a*) and high-speed streak (*b*). The contour interval is 0.025. In (*a*) the $\max(|\langle U_s \rangle|) = 0.21U_c$, $\max(\langle V \rangle) = 0.024U_c$. In (*b*) the $\max(|\langle U_s \rangle|) = 0.16U_c$, $\max(\langle V \rangle) = 0.015U_c$. The contour interval is $0.025U_c$.

Having isolated at each time instant the streamwise-mean R-S with streamwise velocity $U(y, z, t)$, wall-normal velocity $V(y, z, t)$ and spanwise velocity $W(y, z, t)$, we Fourier decompose in the streamwise direction the fluctuation velocities collocated with the streak

$$\boldsymbol{u} = [u(\boldsymbol{x}, t), v(\boldsymbol{x}, t), w(\boldsymbol{x}, t)]^T, \tag{3.1}$$

and calculate the time-mean covariance

$$\boldsymbol{C}_{k_x}(y_1, z_1, y_2, z_2) = \langle \boldsymbol{u}_{k_x}(y_1, z_1) \boldsymbol{u}^{\dagger}_{k_x}(y_2, z_2) \rangle, \tag{3.2}$$

where $\boldsymbol{u}_{k_x}(y_i, z_i))$ is the amplitude of the n_xth Fourier component of the velocity field with streamwise wavenumber, $k_x = n_x\alpha$, at the position (y_i, z_i), with † indicating the Hermitian transpose and $\alpha = 2\pi/L_x$ the smallest streamwise wavenumber in the channel. The same point time-mean covariance is denoted $\boldsymbol{C}_{k_x}(y, z)$. From this time-mean covariance we obtain the time-mean Reynolds stresses produced by the fluctuations.

4. The R-S dynamical balance diagnostics

The time-mean collocated R-S and the associated time-mean collocated fluctuation Reynolds stresses comprise components of the structure of the R-S and the dynamics maintaining it, respectively. We will now examine the terms in this equilibrium for the case of the low-speed streak.

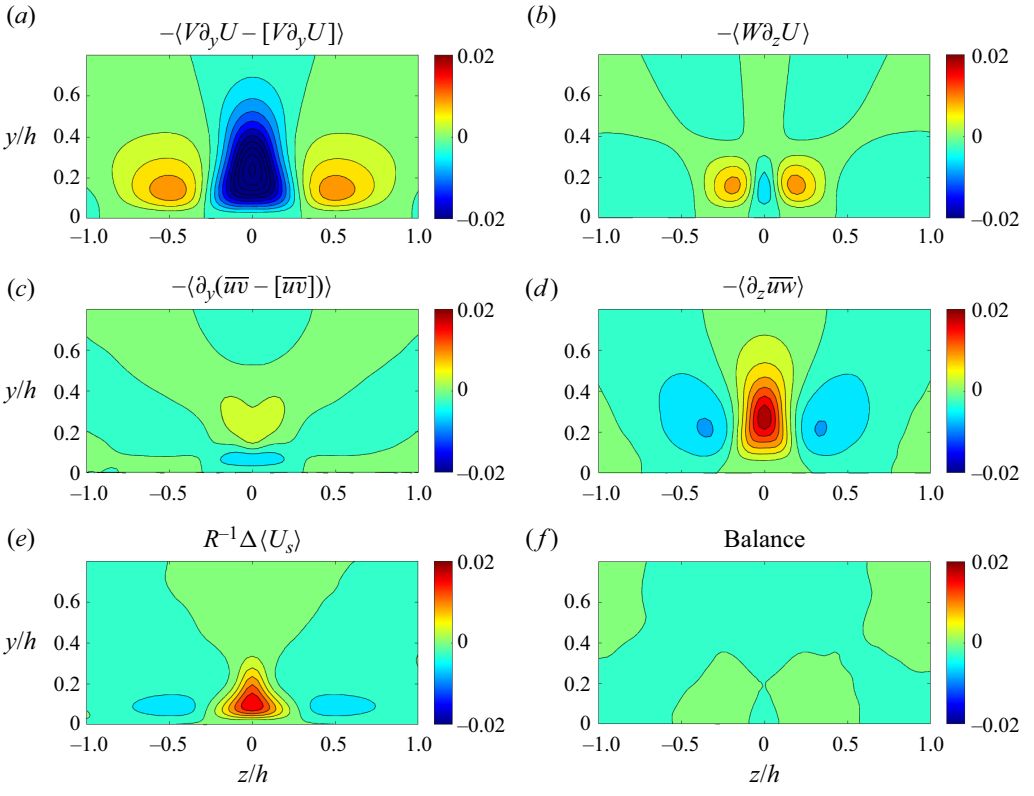

Figure 2. For the low-speed streak in NSE100, contours in the (y, z) plane are shown for (a) $-\langle V\partial_y U - [V\partial_y U]\rangle$, (b) $-\langle W\partial_z U_s\rangle$, (c) $-\langle\partial_y(\overline{uv} - [\overline{uv}])\rangle$, (d) $-\partial_z\langle\overline{uw}\rangle$ and (e) $R^{-1}\Delta\langle U_s\rangle$. The sum shown in (f) confirms that the above terms are in balance. The contour interval is $0.003U_c^2/h$.

Equations (2.1*a*) and (2.2*a*) imply that the streamwise-mean streak, $U_s = U - [U]$, satisfies the equation

$$\partial_t U_s = -(V\partial_y(U) - [V\partial_y U]) - W\partial_z U_s - \partial_y(\overline{uv} - [\overline{uv}]) - \partial_z(\overline{uw} - [\overline{uw}]) + R^{-1}\Delta U_s, \tag{4.1}$$

so that, given that $\partial_z[\overline{uw}] = 0$, the time-mean streak satisfies the force balance:

$$-\langle(V\partial_y(U) - [V\partial_y U])\rangle - \langle W\partial_z U_s\rangle - \partial_y(\langle\overline{uv}\rangle - \langle[\overline{uv}]\rangle) - \partial_z\langle\overline{uw}\rangle + R^{-1}\Delta\langle U_s\rangle = 0. \tag{4.2}$$

The terms comprising this balance are verified to be in a time-mean equilibrium in figure 2, for the NSE100, and in figure 3, for the RNL100. Moreover, figures 2 and 3 show that, in the time-mean, the streak is principally supported by the lift-up mechanism, $-\langle V\partial_y U - [V\partial_y U]\rangle$, and opposed by spanwise Reynolds stress divergence, $-\partial_z\langle\overline{uw}\rangle$ and diffusion $R^{-1}\Delta\langle U_s\rangle$.

A typical time series of the average amplitude of the low-speed streak at the centreline of the streak and of the principal terms in the force balance (4.2) which are the instantaneous average streak acceleration by the lift-up process, $-\int_0^1 \mathrm{d}y(V\partial_y U - [V\partial_y U])$, the average acceleration by spanwise Reynolds stress divergence, $-\int_0^1 \mathrm{d}y\partial_z\overline{uw}$, and the average acceleration due to diffusion, $R^{-1}\int_0^1 \mathrm{d}y\Delta U_s$, are shown in figure 4. The time-mean

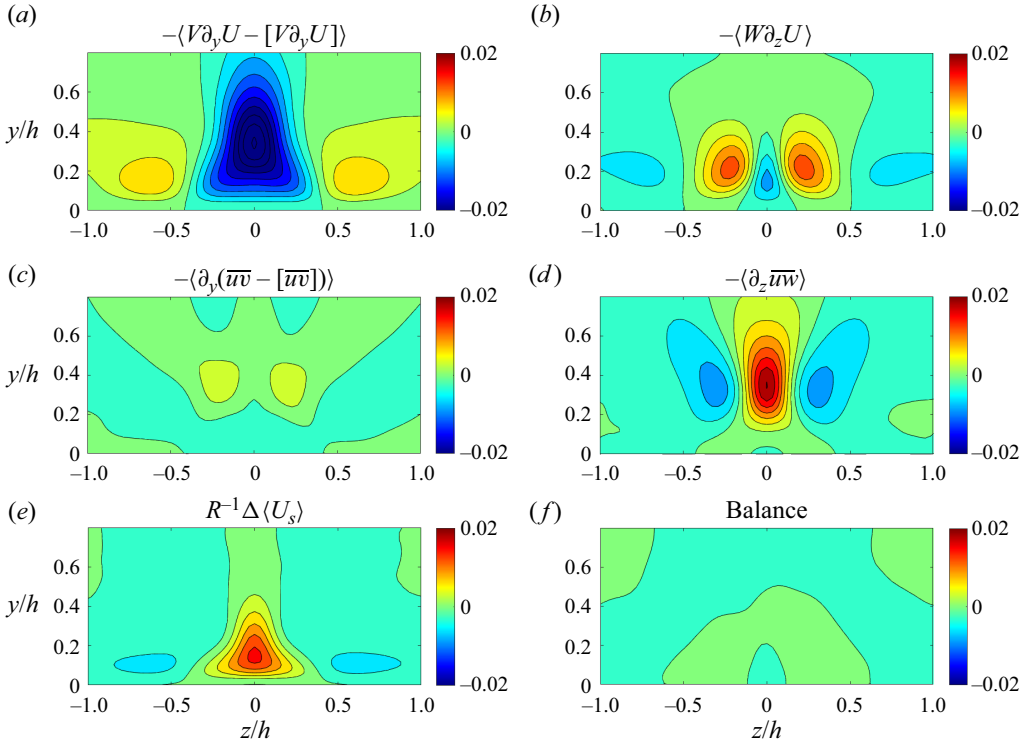

Figure 3. As in figure 2 for RNL100. The contour interval is 0.003 U_c^2/h.

acceleration and standard deviation over the entire dataset due to lift up is $-0.01U_c^2/h$ (dashed blue) with $\sigma = 0.004\ U_c^2/h$, that due to Reynolds stress divergence is $0.007U_c^2/h$ (dashed black) with $\sigma = 0.004U_c^2/h$ and that due to diffusion is $0.003U_c^2/h$ (dashed green) with $\sigma = 0.0013U_c^2/h$. Over the entire dataset the acceleration due to lift up and that due to Reynolds stress divergence, $-\int_0^1 \mathrm{d}y\partial_z\overline{uw}$, are strongly correlated with cross-correlation coefficient 0.72 at lag $1.2h/U_c$ as shown in figure 5. Also, over the entire dataset streak maxima lead the streak regulation term, $-\int_0^h \mathrm{d}y\partial_z(\overline{uw})/(h^2U_c^2)$, by $2h/U_c$. Two bursting events are seen in figure 4 associated with the streak maxima at $3275h/U_c$ and $3866h/U_c$. These streak maxima are followed by maxima of the streak regulation term $-\int_0^h \mathrm{d}y\partial_z(\overline{uw})/(h^2U_c^2)$ at $3282h/U_c$ and $3879h/U_c$, respectively. The near balance and near synchronicity seen in figure 5 indicates that the maintenance and regulation of the streak amplitude is occurring at all times and that breakdown events are not primarily responsible for either the maintenance or the regulation of the streak (see also figure 6).

5. Maintenance of the streamwise-mean roll

Having verified the dominance of lift-up by roll circulations in supporting the R-S, our attention turns to studying the mechanism giving rise to the remarkable universal coincidence in wall turbulence of streaks with roll circulations properly configured to maintain them. By taking the curl of the streamwise-mean equations (2.1*a*) and (2.2*a*) we obtain that in both NSE100 and RNL10 the streamwise component of the vorticity

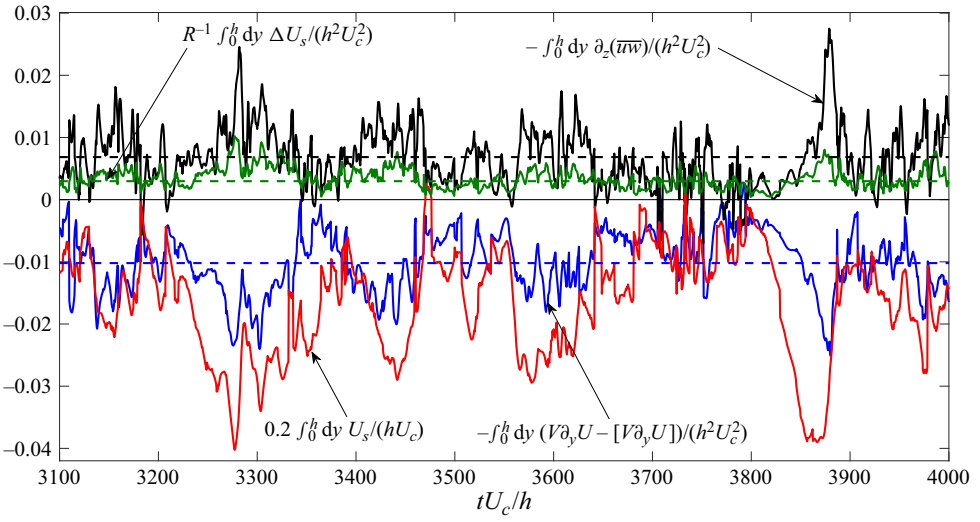

Figure 4. Contributions to streak maintenance and regulation in NSE100. The scaled average streak amplitude at the centreline of the low-speed streak ($0.2\int_0^h \mathrm{d}y U_s/hU_c$) is shown in red. The average streak acceleration by lift-up at the centreline of the low-speed streak ($-\int_0^h \mathrm{d}y(V\partial_y(U)-[V\partial_y U])/(h^2U_c^2)$) (blue) is opposed by the acceleration due to diffusion (green) ($R^{-1}\int_0^h \mathrm{d}y\Delta U_s/(h^2U_c^2)$) and downgradient momentum transport by the streamwise varying fluctuations (black) ($-\int_0^h \mathrm{d}y\partial_z(\overline{uw})/(h^2U_c^2)$). The dashed lines with the corresponding colours indicate the mean values taken over the entire dataset. This figure shows that maintenance and regulation of the streak is occurring continuously in time and is not confined to bursting events.

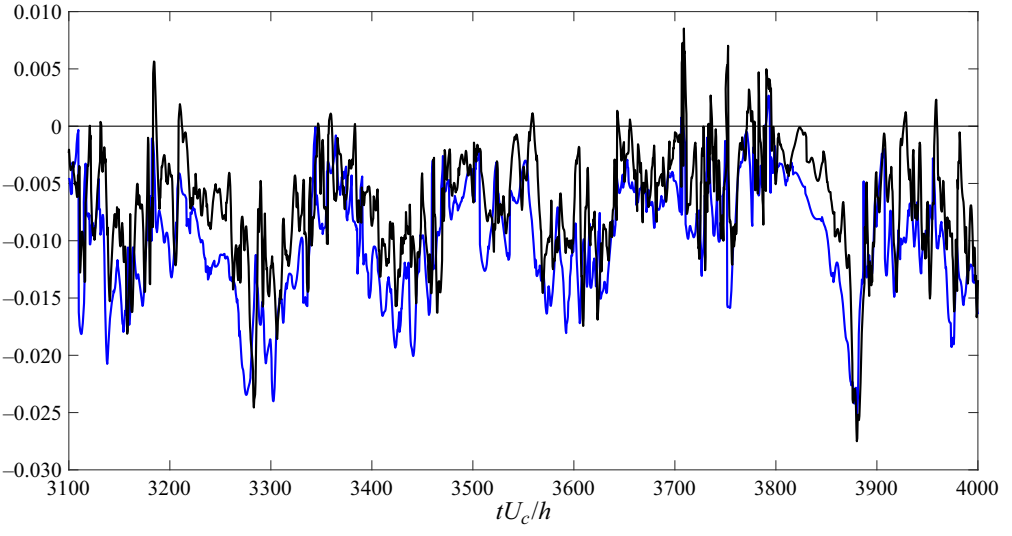

Figure 5. Comparison between the primary components maintaining and regulating the low-speed streak in NSE100. Shown are the acceleration due to lift-up (blue) and the negative of the acceleration due to Reynolds stress divergence (black) (cf. figure 4). The time series have been shifted by the $1.2h/U_c$ lag between them which was obtained over the entire dataset. These two accelerations are highly correlated (correlation coefficient 0.72) revealing that a tight quasiequilibrium between lift-up and downgradient momentum transfer characterizes the maintenance and regulation of the streak amplitude.

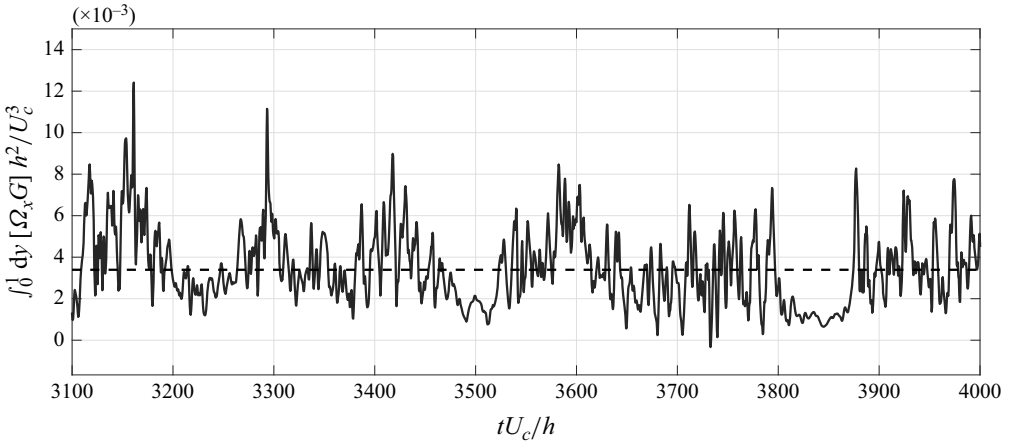

Figure 6. Typical section of the time series of the integrated correlation between the instantaneous value of the streamwise-mean vorticity and the streamwise-mean vorticity source G, $\int_0^1 \mathrm{d}y[\Omega_x G]h^2/U_c^3$, for the case of the low-speed streak in NSE10. Over the whole dataset the time mean is $0.0035h^2/U_c^3$ (dashed). This figure shows that the forcing of the roll, and consequently of the streak, is continuous in time and almost always positive.

$\Omega_x = \partial_y W - \partial_z V$ satisfies the equation

$$\partial_t \Omega_x = \underbrace{-(V\partial_y + W\partial_z)\Omega_x}_{A} + \underbrace{(\partial_{zz} - \partial_{yy})\overline{vw} + \partial_{yz}(\overline{v^2} - \overline{w^2})}_{G} + \underbrace{R^{-1}\Delta\Omega_x}_{D}, \tag{5.1}$$

in which the streamwise-mean wall-normal and spanwise velocities are given by $V = -\partial_z \Delta^{-1}\Omega_x$ and $W = \partial_y \Delta^{-1}\Omega_x$ with the inverse Laplacian Δ^{-1} incorporating the boundary conditions.

The term A, representing advection of Ω_x by the roll velocities (V, W), is not a source of net streamwise vorticity. The roll vorticity is sustained against dissipation, D, by the curl of the force arising from the Reynolds stress divergence, G. In this equation the wall-normal component of the Reynolds stress divergence force is

$$F_y = -\partial_z(\overline{vw}) - \partial_y(\overline{v^2}), \tag{5.2}$$

while the spanwise component is

$$F_z = -\partial_y(\overline{vw}) - \partial_z(\overline{w^2}), \tag{5.3}$$

which results in the contribution to the rate of change of streamwise-mean vorticity in the streamwise direction:

$$G = \widehat{\boldsymbol{x}} \cdot \boldsymbol{\nabla} \times (0, F_y, F_z) = (\partial_{zz} - \partial_{yy})\overline{vw} + \partial_{yz}(\overline{v^2} - \overline{w^2}), \tag{5.4}$$

where $\widehat{\boldsymbol{x}}$ is the unit vector in the streamwise direction. The first right-hand side term in (5.4) represents the contribution to G from the Reynolds shear stress $\overline{vw}$, while the second term represents the contribution from $\overline{v^2} - \overline{w^2}$, which can be identified with anisotropy in the Reynolds normal stress components. The implications of this decomposition are discussed by Alizard *et al.* (2021) in the context of the formation of streamwise constant rolls during transition to turbulence in the RNL framework. The Reynolds normal stress component of G will be shown in the next section to dominate and determine the direction and location of the roll circulation and consequently of the streak acceleration.

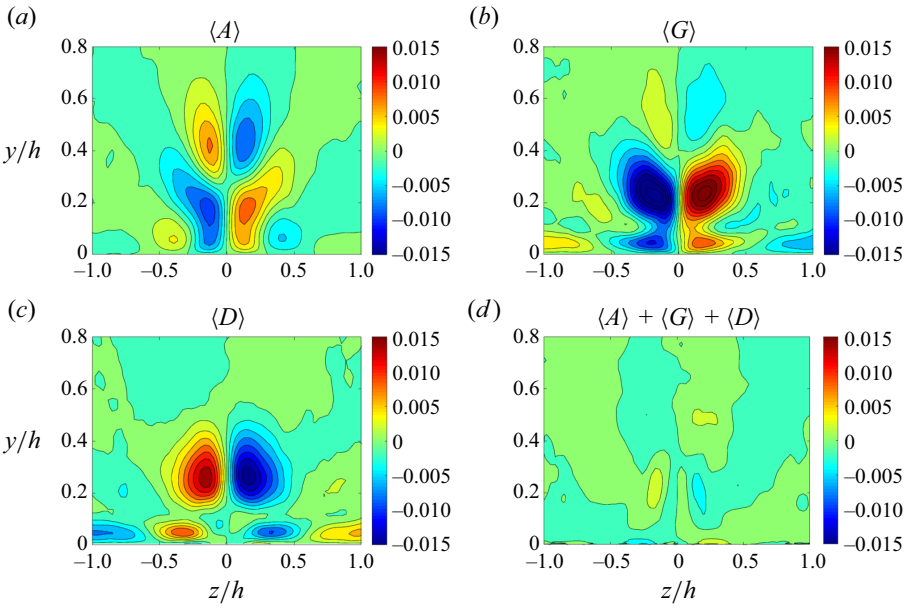

Figure 7. For the low-speed streak in NSE100, contours in the (y, z) plane are shown for (*a*) $\langle A\rangle = -\langle (V\partial_y + W\partial_z)\Omega_x\rangle$, contribution to the time-mean rate of change of $\langle \Omega_x\rangle$ by roll self-advection, (*b*) $\langle G\rangle = (\partial_{zz} - \partial_{yy})\langle \overline{vw}\rangle + \partial_{yz}\langle(\overline{v^2} - \overline{w^2})\rangle$, contribution to the time-mean rate of change of $\langle \Omega_x\rangle$ by Reynolds stress divergence, (*c*) $\langle D\rangle = R^{-1}\Delta\langle \Omega_x\rangle$, contribution to the time-mean rate of change of $\langle \Omega_x\rangle$ by dissipation. The sum shown in (*d*) confirms that the above terms are in balance. The contour interval is $0.0015U_c^2/h$.

A time series of the inner product of Ω_x with G is shown in figure 6. Two observations are appropriate: the first is that roll forcing by Reynolds stresses is continuous in time and almost always positive; the second is that streamwise-mean vorticity forcing is negatively associated with bursting events such as that occurring around $t = 3800$. Continual generation of streamwise vorticity supporting the existing roll circulation both in the buffer layer and also in the logarithmic layer was previously documented in RNL turbulence at Reynolds number $R_\tau = 1000$ (cf. Farrell *et al.* 2016). This result has not yet been confirmed in DNS, but we expect it to be, given that parallel mechanisms underlie wall turbulence in RNL and DNS.

In the time-mean the streamwise-mean vorticity, Ω_x, satisfies the balance

$$\underbrace{-\langle (V\partial_y + W\partial_z)\Omega_x\rangle}_{\langle A\rangle} + \underbrace{(\partial_{zz} - \partial_{yy})\langle \overline{vw}\rangle + \partial_{yz}\langle(\overline{v^2} - \overline{w^2})\rangle}_{\langle G\rangle} + \underbrace{R^{-1}\Delta\langle \Omega_x\rangle}_{\langle D\rangle} = 0. \tag{5.5}$$

The three components of this time-mean balance in NSE100 and RNL100 are shown in figures 7 and 8.

The roll circulation resulting from the forcing by $\langle G\rangle$ can be understood by assessing the wall-normal velocity induced by $\langle G\rangle$ together with its modification by $\langle A\rangle$. The modification given by $\langle A\rangle$ results from a pressure field required so that the circulation forced by $\langle G\rangle$ satisfies boundary conditions. We project (5.5) to streamwise-mean wall-normal velocity by multiplying (5.5) with $-\delta t\partial_z\Delta^{-1}$ for a chosen time interval δt in order to obtain

$$\delta V_A + \delta V_G = -\delta t R^{-1}\Delta\langle V\rangle, \tag{5.6}$$

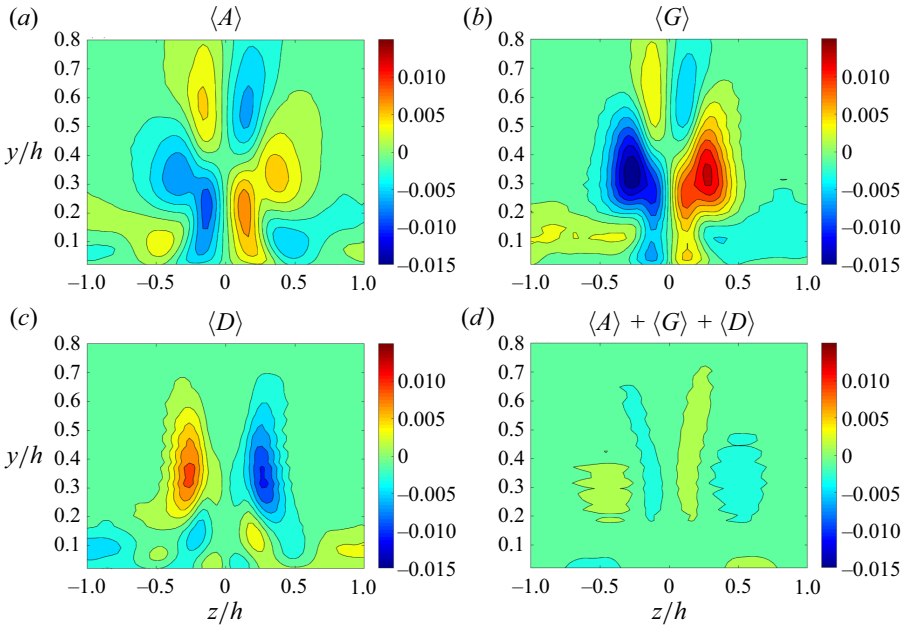

Figure 8. As in figure 7 for RNL100. The contour interval is $0.0015U_c^2/h$.

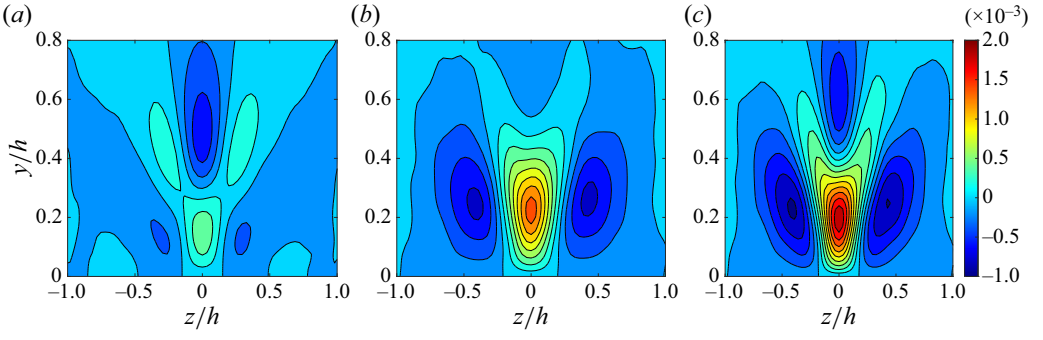

Figure 9. For the low-speed streak in NSE100, contours in the (y, z) plane are shown for (a) the time-mean wall-normal velocity increment resulting from advection, δV_A, (b) the wall-normal velocity increment resulting from Reynolds stress, δV_G, and (c) their sum $\delta V_A + \delta V_G$. This figure shows the contribution of the advection and Reynolds stress to the maintenance of the low-speed R-S. The associated $\langle A\rangle$, $\langle G\rangle$ fields are shown in figure 7(a,b). The contour interval is $2 \times 10^{-4} U_c$.

where $\delta V_G = -\delta t \partial_z \Delta^{-1} \langle G\rangle$ is the wall-normal velocity increment induced by $\langle G\rangle$ over time interval δt and $\delta V_A = -\delta t \partial_z \Delta^{-1} \langle A\rangle$ is the corresponding wall-normal velocity increment induced by $\langle A\rangle$. It is the δV_G induced by $\langle G\rangle$ and corrected by δV_A that determines the equilibrium V field as indicated in the balance equation (5.6). The wall-normal velocity increments δV_G and δV_A maintaining the low-speed R-S in NSE100 are shown in figure 9. This figure shows that δV_G is providing lift-up in the streak core supporting the low-speed R-S and also the corrective δV_A, which is approximately $1/3$ of the δV_G, is adding to the support of the R-S provided by $\langle G\rangle$.

In figure 9 we have taken the time interval for the development of δV to be $\delta t = 1h/U_c$; however, it is instructive to identify a physically relevant value of this time scale which

for the low-speed streak is given by $T_d/\delta t \approx V_{max}/\delta V_{max} = 12$, where V_{max} is the maximum wall normal velocity at the streak centreline (cf. figure 1*a*) and δV_{max} is the maximum wall-normal velocity increment over unit time also evaluated at the centreline (cf. figure 9*c*). This time scale can be interpreted as a Rayleigh damping time scale for equilibration of the roll circulation being forced by the Reynolds stresses.

6. Contribution to roll forcing by the sinuous ($\mathcal{S}$) and varicose ($\mathcal{V}$) fluctuations

In the previous section we showed that the Reynolds stresses induce vorticity forcing that continuously reinforces the pre-existing streamwise-mean streamwise vorticity so as to sustain the R-S. Key to understanding this remarkable property is the dynamics of the $\mathcal{S}$ and $\mathcal{V}$ fluctuations collocated with the mean streak. In this section we isolate the $\mathcal{S}$ and $\mathcal{V}$ components of the velocity fluctuations collocated with the streak and show that the maintenance of the mean R-S can be attributed to the Reynolds stresses due to the $\mathcal{S}$ and $\mathcal{V}$ components of velocity acting independently. Although instantaneous snapshots of the flow field would reveal Reynolds stresses arising from interaction between the $\mathcal{S}$ and $\mathcal{V}$ fields, this interaction vanishes in the time-mean. This is expected because the R-S is mirror-symmetric, and non-vanishing of the time-mean $\mathcal{S}$ and $\mathcal{V}$ covariance would result in Reynolds stresses incompatible with the mirror symmetry of the time-mean R-S – this will be verified below.

In order to define the time-mean covariance of the $\mathcal{S}$ and $\mathcal{V}$ components of the fluctuation field we form at each time step of the simulation the $\mathcal{S}$ and $\mathcal{V}$ components of the velocity field:

$$\boldsymbol{u}_{\mathcal{S}}(x, y, z, t) = \frac{\boldsymbol{u} - \boldsymbol{u}_{mirror}}{2}, \boldsymbol{u}_{\mathcal{V}}(x, y, z, t) = \frac{\boldsymbol{u} + \boldsymbol{u}_{mirror}}{2}, \tag{6.1}$$

in which the mirror symmetric fluctuation field about the plane $z = 0$ is defined as

$$\boldsymbol{u}_{mirror}(x, y, z, t) \stackrel{\text{def}}{=} \begin{pmatrix} u(x, y, -z, t) \\ v(x, y, -z, t) \\ -w(x, y, -z, t) \end{pmatrix}. \tag{6.2}$$

The time-mean spatial covariances of the $\mathcal{S}$ and $\mathcal{V}$ components of the fluctuation field at streamwise wavenumber k_x are $\boldsymbol{C}_{\mathcal{S},k_x}(y_1, z_1, y_2, z_2) \stackrel{\text{def}}{=} \langle \boldsymbol{u}_{\mathcal{S},k_x}(y_1, z_1) \boldsymbol{u}^{\dagger}_{\mathcal{S},k_x}(y_2, z_2) \rangle$ and $\boldsymbol{C}_{\mathcal{V},k_x}(y_1, z_1, y_2, z_2) \stackrel{\text{def}}{=} \langle \boldsymbol{u}_{\mathcal{V},k_x}(y_1, z_1) \boldsymbol{u}^{\dagger}_{\mathcal{V},k_x}(y_2, z_2) \rangle$, where $\boldsymbol{u}_{\mathcal{S}/\mathcal{V},k_x}$ are the Fourier amplitudes of the $\mathcal{S}$ and $\mathcal{V}$ components of the fluctuation velocity field at k_x, while the corresponding covariance of the total field is given by $\boldsymbol{C}_{k_x}(y_1, z_1, y_2, z_2) \stackrel{\text{def}}{=} \langle \boldsymbol{u}_{k_x}(y_1, z_1) \boldsymbol{u}^{\dagger}_{k_x}(y_2, z_2) \rangle$. The asymptotic approach in time of the equality

$$\boldsymbol{C}_{k_x}(y_1, z_1, y_2, z_2) = \boldsymbol{C}_{\mathcal{S},k_x}(y_1, z_1, y_2, z_2) + \boldsymbol{C}_{\mathcal{V},k_x}(y_1, z_1, y_2, z_2) \tag{6.3}$$

has been verified, implying that there is no time-mean correlation between the $\mathcal{S}$ and $\mathcal{V}$ fluctuations. Consequently, the time-mean fluctuation Reynolds stresses, which are a linear function of the covariances, are the sum of the Reynolds stresses obtained from the respective $\mathcal{S}$ and $\mathcal{V}$ covariances. The fluctuation Reynolds stress can be further partitioned into a sum over k_x. Using this partition into $\mathcal{S}$ and $\mathcal{V}$ components at each wavenumber k_x, we can separate the contribution of the $\mathcal{S}$ and $\mathcal{V}$ components at each k_x to the mechanism sustaining the R-S.

We turn now to study how the roll is induced by the time-mean fluctuation Reynolds stresses. We first consider the contribution to the roll forcing by the time-mean Reynolds

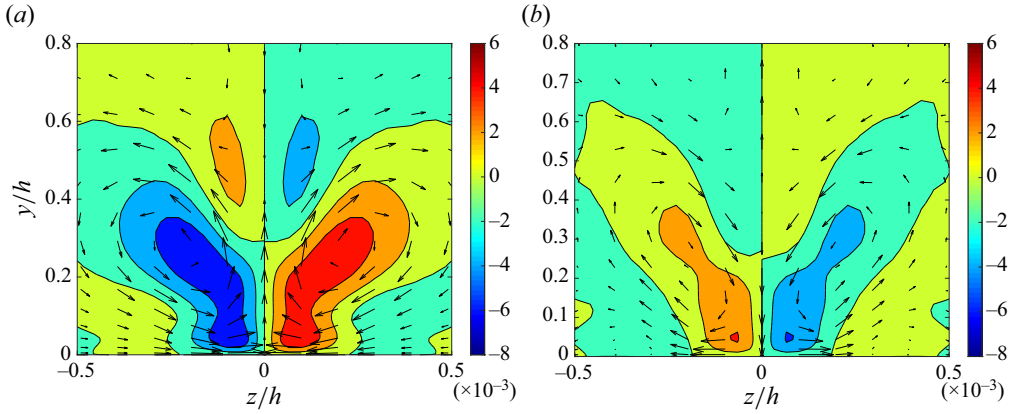

Figure 10. Increment of mean streamwise vorticity, $\delta\Omega_{x,k_x}$, induced over unit time by Reynolds stresses of the $\mathcal{S}$ (*a*) and the $\mathcal{V}$ (*b*) $k_x/\alpha = 3$ fluctuations in the low-speed streak of NSE100. Wavenumber $k_x/\alpha = 3$ is chosen because the forcing is maximized at this wavenumber (cf. figure 12*a*). Also shown are vectors with components $(\delta W_{k_x}, \delta V_{k_x})$. This figure shows that the $\mathcal{S}$ fluctuations reinforce the low-speed streak while the $\mathcal{V}$ fluctuations oppose it. Overall the $\mathcal{S}$ fluctuations are dominant and the low-speed streak is sustained.

stresses due to k_x fluctuations, $\langle G_{k_x}\rangle = (\partial_{zz} - \partial_{yy})\langle\overline{vw}\rangle_{k_x} + \partial_{yz}\langle(\overline{v^2} - \overline{w^2})\rangle_{k_x}$. This $\langle G_{k_x}\rangle$ acting alone would result, as discussed in the previous section, in a wall-normal velocity increment over time δt, $\delta V_{k_x} = -\delta t\partial_z\Delta^{-1}\langle G_{k_x}\rangle$, and a spanwise velocity increment over time δt, $\delta W_{k_x} = \delta t\partial_y\Delta^{-1}\langle G_{k_x}\rangle$. The associated streamwise-mean vorticity increment is $\delta\Omega_{x,k_x} = \langle G_{k_x}\rangle\delta t$ and Δ^{-1} the inverse Laplacian required to account for the influence of pressure forces arising from the boundary conditions. We choose $\delta t = 1$ from now on.

The spatial distribution of $\delta\Omega_{x,k_x}$ and vector plots of the streamwise-mean velocity fields $(\delta V_{k_x}, \delta W_{k_x})$ induced by $\mathcal{S}$ and $\mathcal{V}$ components of $k_x = 3\alpha$ fluctuations in NSE100 for the case of the low-speed streak are shown in figure 10. Note that the velocity increment vectors are not tangent to the contours of the vorticity increments, $\delta\Omega_{x,k_x}$. This is due to the action of pressure forces arising due to the boundary conditions. This figure demonstrates that $\mathcal{S}$ Reynolds stresses produce mean vorticity that reinforces the low speed streak while the $\mathcal{V}$ Reynolds stresses oppose the low-speed streak. In low-speed streaks the $\mathcal{S}$ Reynolds stresses dominate, consistent with the $\mathcal{S}$ structures maintaining the low-speed streak. While both $\mathcal{S}$ and $\mathcal{V}$ fluctuations are present in association with low-speed streaks so that application of targeted data analysis techniques could be used to deduce the presence of, for example, hairpin vortex structures in association with low-speed streaks, this result demonstrates that the varicose component at $k_x = 3\alpha$ opposes rather than maintains the low-speed streak. We will verify that this is also the case at other k_x. Conversely, in high-speed streaks the $\mathcal{V}$ Reynolds stresses dominate, consistent with maintaining the high-speed streak. We will show that this is also a general property. In RNL100 we obtain similar results (cf. figure 11).

The velocity increment forced by the Reynolds stresses over the primary area of lift-up forcing (see figure 9*b*)

$$\widetilde{\delta V}_{k_x} \stackrel{\text{def}}{=} \int_{-z_0}^{z_0} \frac{\mathrm{d}z}{2z_0} \int_0^{y_0} \frac{\mathrm{d}y}{y_0} \delta V_{k_x}(y, z), \tag{6.4}$$

with $y_0 = h/2$ and $z_0 = 0.26h$, partitioned into $\mathcal{S}$ and $\mathcal{V}$ components, and the velocity increment induced by their sum, $\mathcal{S} + \mathcal{V}$, as a function of the streamwise wavenumber of the fluctuations, k_x/α, for the case of the low-speed streak and the high-speed streak in

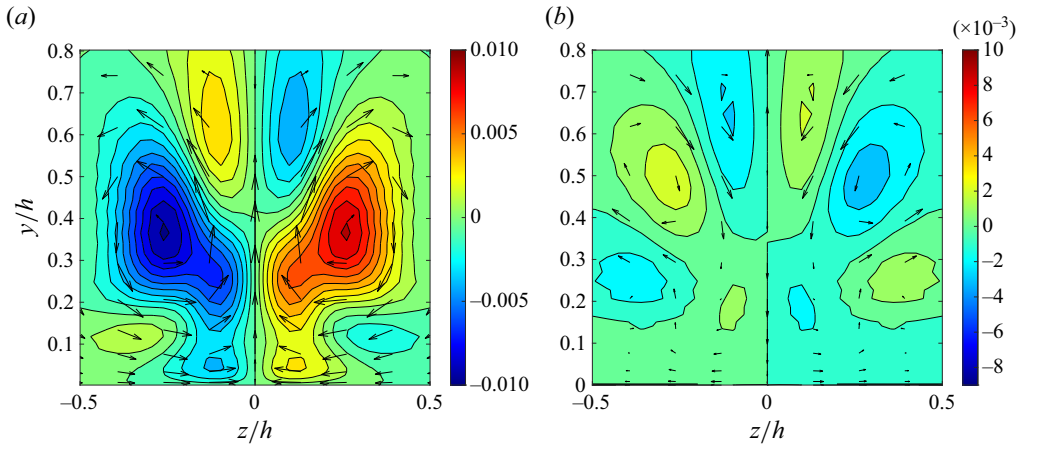

Figure 11. Increment of mean streamwise vorticity, $\delta\Omega_{x,k_x}$, induced over unit time by Reynolds stresses of the $\mathcal{S}$ (*a*) and the $\mathcal{V}$ (*b*) $k_x/\alpha = 2$ fluctuations that are collocated with the mean low-speed streak in RNL100. Wavenumber $k_x/\alpha = 2$ is chosen because the forcing is maximized at this wavenumber (cf. figure 13*a*). Also shown are vectors with components the roll velocities induced over unit time $(\delta W_{k_x}, \delta V_{k_x})$. This figure shows that the $\mathcal{S}$ fluctuations reinforce the low-speed streak while the $\mathcal{V}$ fluctuations oppose it as in NSE100 shown in figure 10.

NSE100 is shown in figure 12. The corresponding RNL100 results shown in figure 13 are similar to those of the NSE100, except that in RNL100 the streak is supported by only the first three streamwise wavenumbers, which are the streamwise wavenumbers spontaneously retained by RNL dynamics. These figures show that in the time-mean and at all streamwise wavenumbers considered, the $\mathcal{S}$ fluctuations induce lift-up in both low- and high-speed streaks, while the $\mathcal{V}$ induce push-down. These figures also show that in low-speed streaks the $\mathcal{S}$ component dominates the $\mathcal{V}$ at every k_x resulting in the support of the low-speed streak, while in high-speed streaks the $\mathcal{V}$ component dominates the $\mathcal{S}$ resulting in the support of the high-speed streak. Also the contribution to roll forcing by the fluctuations at each wavenumber is similarly distributed so that each wavenumber is contributing to the reinforcement of the pre-existing R-S. Note that the Reynolds stress induced time-mean $\widetilde{\delta V}_{k_x}$ is maximized at $k_x/\alpha = 3$ for both low-speed and high-speed streaks in NSE100. However, the support of the streak extends over a broad band of streamwise wavenumbers implying structural robustness of the mechanism of roll forcing supporting the SSP cycle in wall turbulence.

Note that the wall-normal velocity increments induced either by the $\mathcal{S}$ or the $\mathcal{V}$ fluctuations in the case of the low-speed streak are substantially larger than the corresponding velocity increments induced for the case of the high-speed streak. Moreover, the net roll forcing from the sum of the opposing $\mathcal{S}$ and $\mathcal{V}$ induced velocities is approximately two times larger in the low-speed streak compared with the high-speed streak. This dynamical advantage in forcing of the low-speed streak in comparison with the forcing of the high-speed streak, combined with the increased dissipation resulting from displacement of the high-speed streak towards the boundary, provides explanation for the relative dominance of the low-speed streak in observations of isolated R-S as occur in this Poiseuille flow. In the case of the highly ordered R-S observed in wide channel Couette flow (Pirozzoli *et al.* 2014), the low- and high-speed streaks would not be independent and their interaction would need to be taken into account.

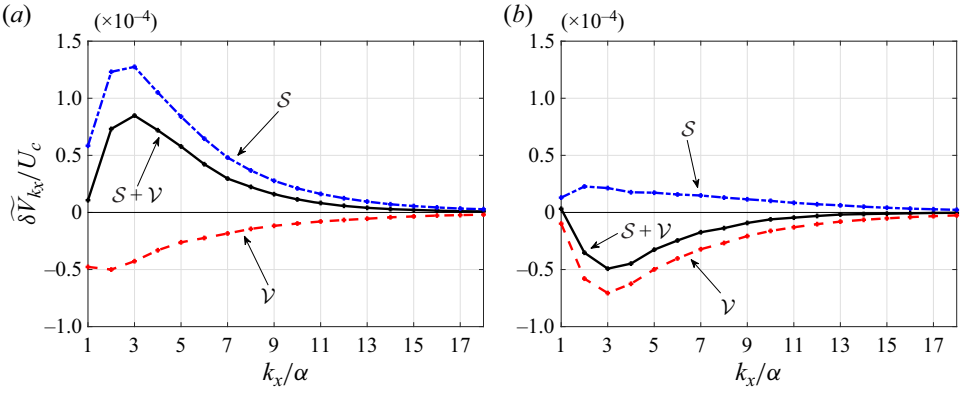

Figure 12. Velocity increments, $\widetilde{\delta V}_{k_x}$, forced by the Reynolds stresses over the primary area of lift-up, partitioned into $\mathcal{S}$ and $\mathcal{V}$ components, and the velocity increment induced by their sum, $\mathcal{S}+\mathcal{V}$, as a function of the streamwise wavenumber of the fluctuations, k_x/α, for the case of the low-speed streak (*a*) and the high-speed streak (*b*) of NSE100. The largest induced velocity occurs at $k_x/\alpha = 3$ for both the low-speed streak and high-speed streak. These figures show that in the time-mean the $\mathcal{S}$ fluctuations induce lift-up while the $\mathcal{V}$ induce push-down. In the low-speed streak the $\mathcal{S}$ induced lift-up dominates the $\mathcal{V}$ push-down producing maintenance of the low-speed streak, while in the high-speed streak the $\mathcal{V}$ induced lift-up dominates the $\mathcal{S}$ push-down producing maintenance of the high-speed streak.

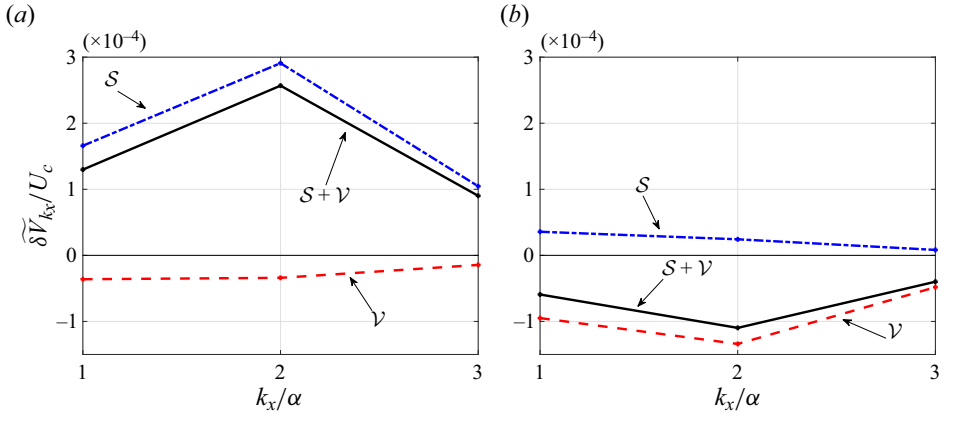

Figure 13. As in figure 12 except RNL100.

7. Contribution to streak forcing by the $\mathcal{S}$ and $\mathcal{V}$ shear and normal Reynolds stress components

Simplicity in analysing the mechanism by which the Reynolds stress forcing G gives rise to the R-S can be obtained by concentrating on the forcing of V along the centreline of the streak given by $\delta V_{k_x}(y, z = 0)$. The y structure of the $\mathcal{S}$ and $\mathcal{V}$ components of $\delta V_{k_x}(y, z = 0)$ for the low-speed streak in NSE100 is shown in figure 14. This figure shows that the Reynolds stress induced lift-up at each wavenumber add coherently.

For the analysis of the streak forcing we choose to show the streak velocity at the streak centreline induced by $\delta V_{k_x}(y, 0)$ acting over unit time, $\delta U = -\delta V_{k_x}(y, 0)U'(y, 0)\delta t$, with $\delta t = 1$ and $U'(y, 0)$ the shear of the streamwise flow at the streak centreline. The streak velocity δU induced by the dominant $k_x/\alpha = 3$ fluctuations is plotted in figure 15 for the low-speed streak in NSE100 and in figure 16 for the high-speed streak in NSE100,

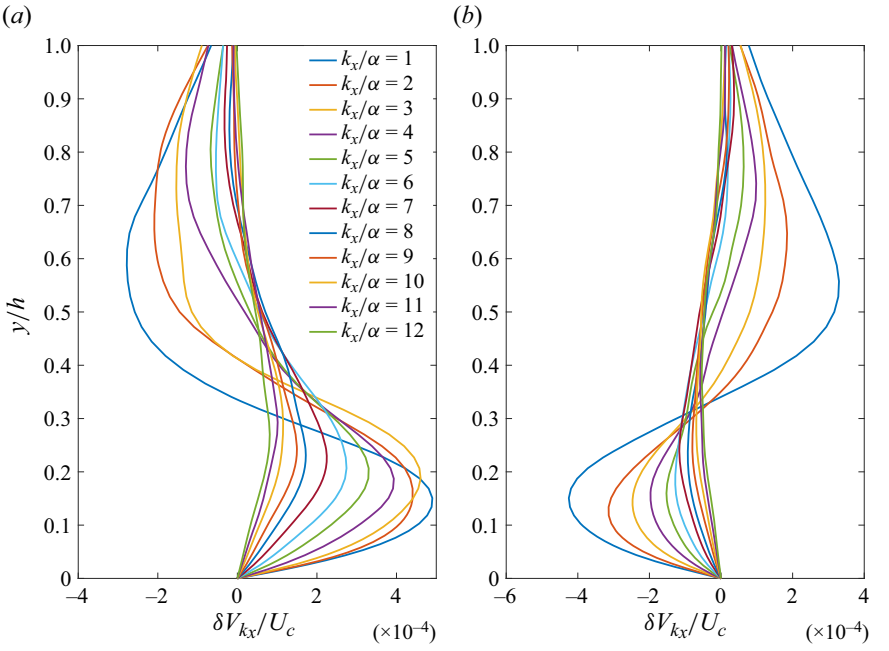

Figure 14. Wall-normal distribution at the centreline of $\delta V_{k_x}(y, z = 0)$. Shown separately are the $\mathcal{S}$ (*a*) and the $\mathcal{V}$ (*b*) components with streamwise wavenumber $k_x/\alpha = 1, 2, \ldots, 12$ for the case of the low-speed streak of NSE100.

both of which are located in the lower half of the channel by our collocation procedure. The net δU induced in the upper half of the channel by the $\mathcal{S}$ and $\mathcal{V}$ fluctuations, where there is no streak, vanishes in the time-mean. In the lower region, where there is a streak, the $\mathcal{S}$ and $\mathcal{V}$ contributions do not cancel in the time-mean and a net δU results. In the low-speed streak region of figure 15(*a*), the $\mathcal{S}$ fluctuations dominate the $\mathcal{V}$ fluctuations in the time-mean resulting in δU increments supporting the low-speed streak. In general it can be shown that $\mathcal{S}$ fluctuations force low-speed streaks while $\mathcal{V}$ fluctuations oppose this forcing (Farrell, Ioannou & Nikolaidis 2022). In the high-speed streak regions, as shown in figure 16(*a*), the high-speed streak is forced by the Reynolds stresses of $\mathcal{V}$ fluctuations which dominate the opposing tendency of the $\mathcal{S}$ fluctuations. The induced δU in RNL100 are similar; for example, in figure 17 we show the induced δU by the $k_x/\alpha = 2$ fluctuations in the low-speed streak in the lower half of the channel of RNL100 and the δU in the spanwise uniform flow in the upper half of the channel.

Partition of the Reynolds stress induced streak increment δU into the component δU_{vw} induced by the Reynolds shear stresses, $\langle \overline{vw} \rangle$, and that induced by the Reynolds normal stresses, $\langle \overline{v^2 - w^2} \rangle$ is shown in figures 15(*b*,*c*), 16(*b*,*c*) and 17(*b*,*c*). The net dynamically relevant asymmetric normal stress, $\langle \overline{v^2 - w^2} \rangle$, which results from the dominance of the $\mathcal{S}$ over the $\mathcal{V}$ fluctuations in the presence of a low-speed streak, is seen to determine the resulting net streak forcing. Moreover, similar distributions characterize the induced acceleration for other streamwise wavenumbers, k_x. This will be shown below to be a consequence of universality in the structure of the Reynolds-stress with k_x.

Indicative of the primary dynamics underlying the R-S is the Reynolds normal stress produced by the dominant wavenumbers. The distribution of the time-mean Reynolds normal stress components partitioned into the contribution from the $\mathcal{S}$ and the $\mathcal{V}$

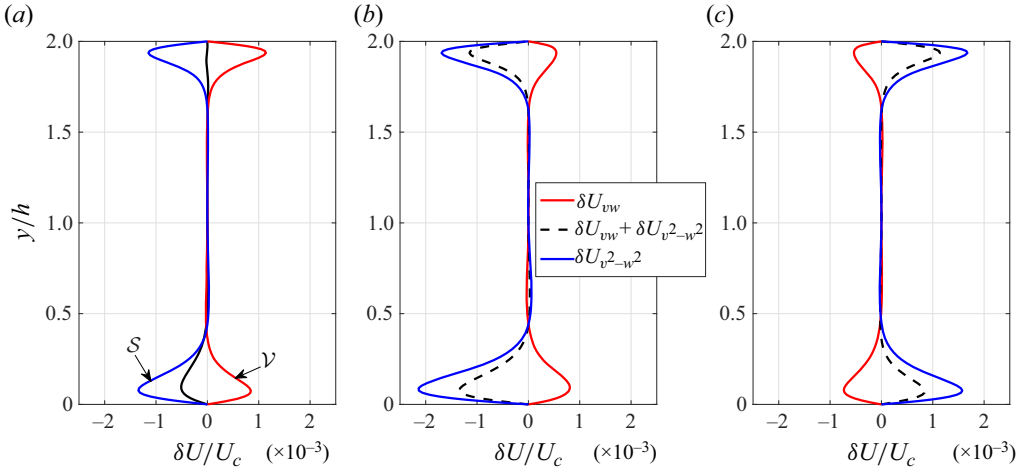

Figure 15. In (*a*) is shown the contribution to streak forcing, δU, that is induced by lift-up. The lift-up is that induced over unit time by the $k_x/\alpha = 3$ fluctuations. Shown is the resulting δU in the low-speed streak region ($y/h < 1$) and in the spanwise uniform flow ($y/h > 1$) in NSE100 (black). Shown separately are contributions to δU induced by the $\mathcal{S}$ (blue) and $\mathcal{V}$ fluctuations (red). In (*b*) is shown partition of the δU induced by $\mathcal{S}$ (dashed black) into the component, $\delta U_{v^2-w^2}$, induced by the $\langle \overline{v^2 - w^2} \rangle$ Reynolds stresses (solid blue) and the component, δU_{vw}, induced by the $\langle \overline{vw} \rangle$ Reynolds stresses (solid red) while in (*c*) is shown the corresponding partition for the $\mathcal{V}$ fluctuations. This figure shows that $\mathcal{S}$ fluctuations tend to accelerate the low-speed streaks, while the $\mathcal{V}$ fluctuations tend to decelerate it; that the acceleration induced by the $\mathcal{S}$ is greater than that induced by the $\mathcal{V}$ in the region of the low-speed streak in the lower half of the channel; that the $\mathcal{S}$ and $\mathcal{V}$ accelerations are equal and opposite where there is no streak; that the $\langle \overline{v^2 - w^2} \rangle$ Reynolds normal stress dominates the forcing of lift-up resulting in streak forcing, δU. Here (*a*) $\mathcal{S} + \mathcal{V}$, (*b*) $\mathcal{S}$ and (*c*) $\mathcal{V}$.

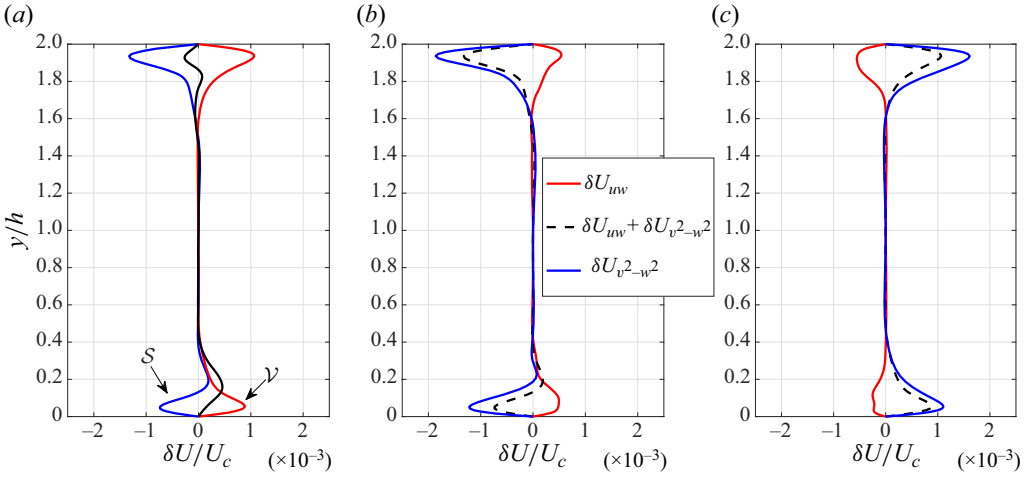

Figure 16. As in figure 15 except for the $k_x/\alpha = 3$ fluctuations in the high-speed streak in NSE100. Here (*a*) $\mathcal{S} + \mathcal{V}$, (*b*) $\mathcal{S}$ and (*c*) $\mathcal{V}$.

fluctuations and the sum of these is shown in figure 18. The $\mathcal{S}$ fluctuations have $v = 0$ and $\partial_z w = 0$ at the centreline and the normal stress asymmetric component $\langle \overline{v^2 - w^2} \rangle$ is negative and has a minimum as a function of z at the centreline with its overall minimum, in the case of our streak, attained at $y/h \approx 0.4$ above the centre of the streak, which is

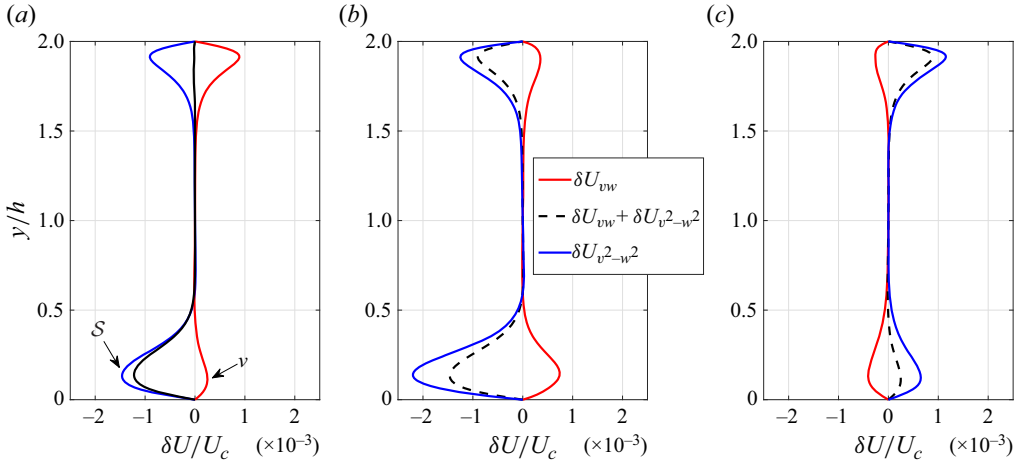

Figure 17. As in figure 15 except for the $k_x/\alpha = 2$ fluctuations in the low-speed streak in RNL100. Here (*a*) $\mathcal{S}+\mathcal{V}$, (*b*) $\mathcal{S}$ and (*c*) $\mathcal{V}$.

at $y/h \approx 0.15$ (cf. figures 1*a* and 18*a*). The $\mathcal{V}$ fluctuations have $w = 0$ and $\partial_z v = 0$ at the centreline consistent with maxima of $\langle\overline{v^2 - w^2}\rangle$ at the centre of the streak (cf. figure 18*b*). In the absence of a streak, as in the region of the upper boundary of the channel, the $\mathcal{S}$ fluctuations and the $\mathcal{V}$ fluctuations are equal and the sum $\langle\overline{v^2 - w^2}\rangle$ is constant in the spanwise direction, as shown in figure 18(*c*) near the upper boundary, and no roll forcing results from the Reynolds normal stress. In low-speed streaks, as in the region of the lower boundary of the channel, the $\mathcal{S}$ fluctuations dominate consistent with the primacy of this term in providing the required roll forcing to maintain the low-speed streak through lift-up (cf. figure 18*c*). In contrast to the case of low-speed streaks, in high-speed streaks the $\mathcal{V}$ fluctuations dominate with the maximum $\langle\overline{v^2 - w^2}\rangle$ of the $\mathcal{V}$ fluctuations almost cancelling the minimum of the $\mathcal{S}$ fluctuations at the centreline leading the total $\langle\overline{v^2 - w^2}\rangle$ to be determined by the two minima of $\langle\overline{v^2 - w^2}\rangle$ of the $\mathcal{V}$ fluctuations at the wings of the streak (cf. figure 19). Note that the stresses in the presence of a high-speed streak are not mirror images of the stresses in the presence of a low-speed streak as the low-speed streak flow is not a mirror image of the high-speed streak flow. However, as discussed in the next section, the stresses in the presence of infinitesimal low- and high-speed streaks are mirror images of each other and remarkably the low-speed streak is dominantly forced by the $\mathcal{S}$ fluctuations and the high-speed streak by $\mathcal{V}$ fluctuations even for infinitesimal strain of the perturbation field. The high-speed streak is supported by the $\langle\overline{w^2}\rangle$ component of the normal stress at the wings of the high-speed streak, consistent with the $\langle\overline{w^2}\rangle$ Reynolds stress distribution being the dominant component supporting both low- and high-speed streaks. A similar dominance of the $\overline{w^2}$ component of the normal stress in roll formation was found in transitional RNL flows by Alizard *et al.* (2021) and in the vortex-wave theory for the generation of rolls (cf. Hall & Sherwin 2010).

The crucial observation is that in the region of the streak an asymmetry between the $\mathcal{S}$ and $\mathcal{V}$ induces net Reynolds stresses that sustain the pre-existing streak. This asymmetry between $\mathcal{S}$ and $\mathcal{V}$ fluctuations arises as a general property of turbulence in the presence of a streak, as will be argued in the next section, and manifests in the time-mean statistics as a general property that is responsible for the roll forcing that generates and maintains

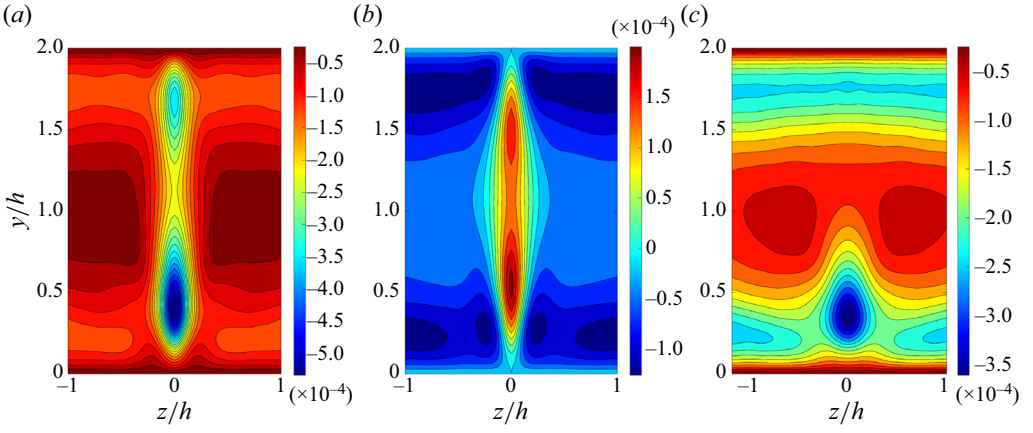

Figure 18. Time-mean Reynolds normal stress at $k_x/\alpha = 3$ in NSE100 for the low-speed streak shown in figure 1. The normal stress shown is partitioned into (*a*) $\mathcal{S}$ and (*b*) $\mathcal{V}$ components. (*c*) The total time-mean normal stress is the sum of $\mathcal{S} + V$. This figure shows that the low-speed streak results primarily from the $\mathcal{S}$ component. Near the upper boundary the flow is spanwise homogeneous and the normal stress becomes spanwise constant producing no roll-forcing. The contour interval is $0.25 \times 10^{-4}\, U_c^2$. Here (*a*) $\overline{(v^2 - w^2)}_{k_x=3\alpha}$ of $\mathcal{S}$, (*b*) $\overline{(v^2 - w^2)}_{k_x=3\alpha}$ of $\mathcal{V}$ and (*c*) $\overline{(v^2 - w^2)}_{k_x=3\alpha}$ of $\mathcal{S} + V$.

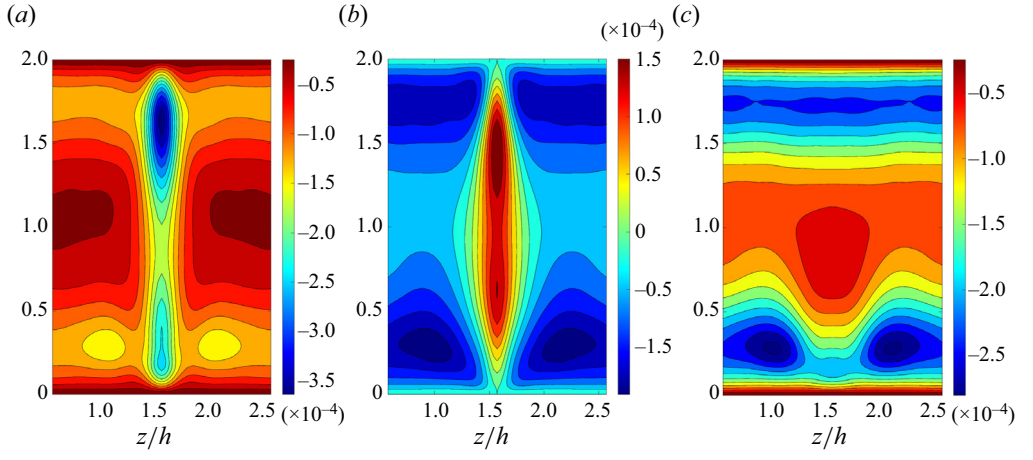

Figure 19. As in figure 18 except for the high-speed streak. Here (*a*) $\overline{(v^2 - w^2)}_{k_x=3\alpha}$ of $\mathcal{S}$, (*b*) $\overline{(v^2 - w^2)}_{k_x=3\alpha}$ of $\mathcal{V}$ and (*c*) $\overline{(v^2 - w^2)}_{k_x=3\alpha}$ of $\mathcal{S} + V$.

the SSP and that underlies the universal mechanism of the S3T modal instability of spanwise uniform mean flows in the presence of background turbulence responsible for the emergence of the R-S as a ubiquitous structure in turbulent shear flows (Farrell & Ioannou 2012; Farrell *et al.* 2017*b*, 2022).

8. Universality in structure of the Reynolds stresses arising from fluctuations about the mean streak

We have seen that the SSP is primarily supported by the Reynolds stresses of the first 10 streamwise wavenumbers (cf. figure 12). The time-mean Reynolds stresses at these

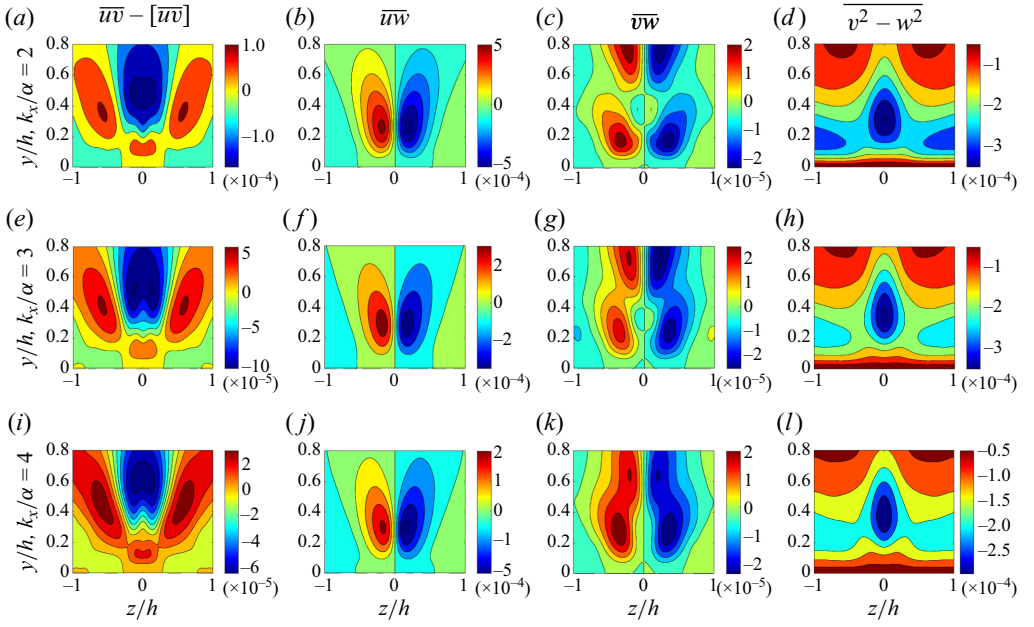

Figure 20. Time-mean Reynolds stresses of fluctuations collocated with low-speed streak of NSE100. Here (*a–d*) $k_x/\alpha = 2$; (*e–h*) $k_x/\alpha = 3$; (*i–l*) $k_x/\alpha = 4$. Panels (*a*,*b*,*e*,*f*,*i*,*j*) show contours of $\langle \overline{uv} - [\overline{uv}] \rangle$ and $\langle \overline{uw} \rangle$ which comprise the Reynolds stresses responsible for the regulation of the streak. Panels (*c*,*d*,*g*,*h*,*k*,*l*) show contours of $\langle \overline{vw} \rangle$ and $\langle \overline{v^2 - w^2} \rangle$ which comprise the Reynolds stresses responsible for forcing the roll sustaining the low-speed streak. This figure shows that there is universality in the mechanism sustaining and regulating the low-speed streak as a function of streamwise wavenumber.

wavenumbers exhibit a notable universality in structure about the time-mean streak for the case of both the low-speed streak (figures 20 and 21) and the high-speed streak (figure 22). Universality and self-similarity of the time-mean structure of fluctuations about time-mean flows has been found to characterize wall-bounded turbulence (del Álamo *et al.* 2006; Hwang & Cossu 2010; Lozano-Durán & Jiménez 2014; Hwang 2015; Hellström, Marusic & Smits 2016) and it has been demonstrated that this property derives from the linear interaction of the fluctuations with the time-mean flow (Farrell & Ioannou 1993*a*; del Álamo & Jiménez 2006; Moarref *et al.* 2013; McKeon 2019; Vadarevu *et al.* 2019; Hwang & Eckhardt 2020; Holford & Hwang 2023). Here we verify the universality of the time-mean structure of the large-scale fluctuations that are collocated with the low-speed and high-speed streak, which was already apparent in figure 14, and attribute the self-similarity of these structures to the linear interaction of the fluctuations with the time-mean streak. The typical structure of Reynolds stresses of the fluctuations in NSE100 in low-speed streaks is shown in figure 20 and for high-speed streaks in figure 22. These figures show the universality in streamwise wavenumber of the structure of the time-mean Reynolds stresses implying universality of the mechanism sustaining and regulating both the low- and high-speed streaks. Remarkably, the universal structure of the fluctuations on the streak will be shown to arise from the growth of fluctuations excited white-in-energy so that their structure arises solely from the optimal growth properties of the streak and does not require the introduction of colour to the excitation.

The structure of the $\langle \overline{uw} \rangle$ (figures 20*b*,*f*,*j*, 21*b*,*f*,*j* and 22*b*,*f*,*j*) and of the $\langle \overline{v^2 - w^2} \rangle$ (figures 20*d*,*h*,*l*, 21*d*,*h*,*l* and 22*d*,*h*,*l*) Reynolds stress components are directly interpretable.

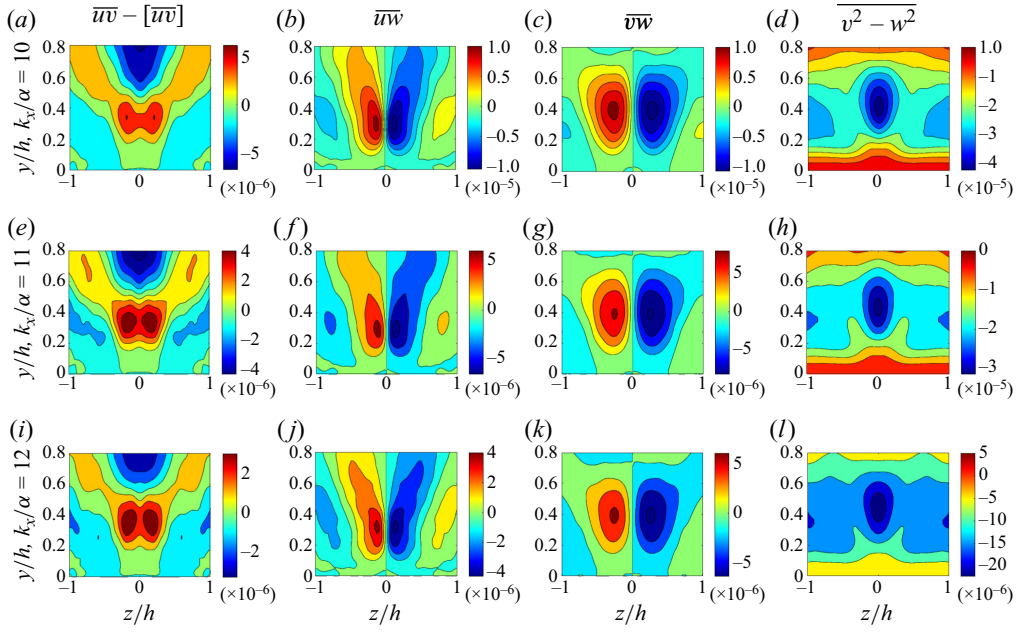

Figure 21. As in figure 20 for fluctuations with $k_x/\alpha = 10$ (*a–d*), $k_x/\alpha = 11$ (*e–h*) and $k_x/\alpha = 12$ (*i–l*). This figure shows that the universality in structure is still apparent at high streamwise wavenumbers.

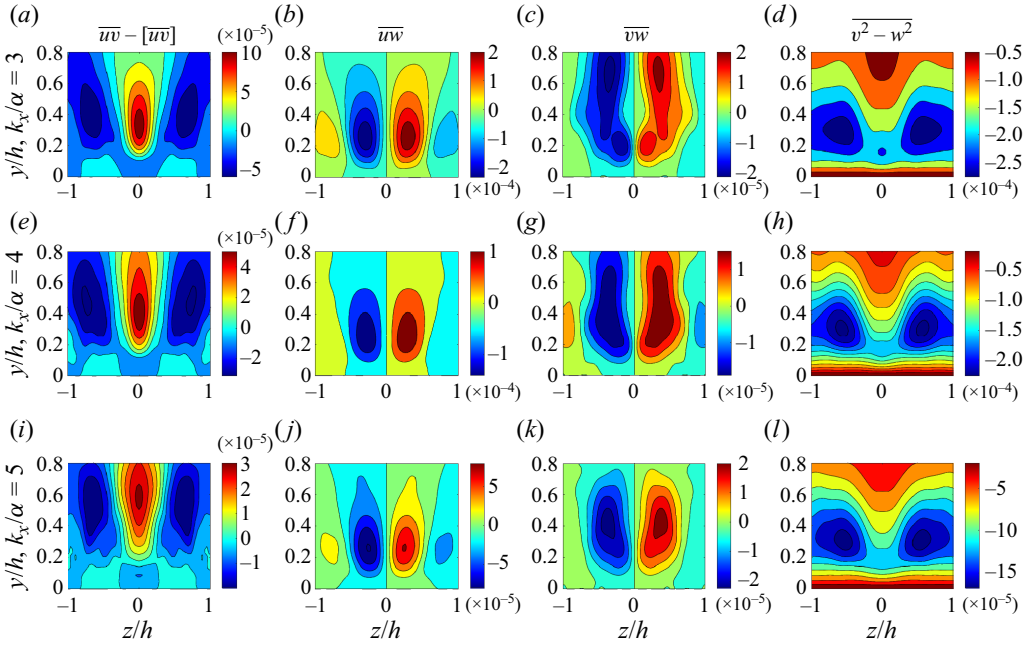

Figure 22. As in figure 20 except for fluctuations with $k_x/\alpha = 3$ (*a–d*), $k_x/\alpha = 4$ (*e–h*) and $k_x/\alpha = 5$ (*i–l*) in the high-speed streak.

The structure of $\langle\overline{uw}\rangle$ indicates that energy is being transferred in the mean from the spanwise varying mean streak to the fluctuations. This reflects the mechanism by which the fluctuations are sustaining while at the same time regulating the streaks. Near the centreline of a low-speed streak $\partial_z\langle\overline{uw}\rangle < 0$ indicating that on average the fluctuations are being sustained by gaining kinetic energy from the streak (cf. figure 20*b*,*f*,*j*). The opposite polarity of the $\langle\overline{uw}\rangle$ is found as required for sustaining the fluctuations in the case of a high speed streak (cf. figure 22*b*,*f*,*j*). The $\langle\overline{v^2 - w^2}\rangle$ Reynolds stress, identified as the asymmetric component of the Reynolds normal stress, was shown above to be the primary source of roll acceleration supporting the streak through the lift-up mechanism. As discussed in the previous section the minimum of the normal stress at the centreline of the low-speed streak indicates dominance of the $\mathcal{S}$ component of the fluctuations, consistent with the primacy of this term in providing the roll forcing maintaining the low-speed streak through lift-up (cf. figures 20*d*,*h*,*l* and 21*d*,*h*,*l*). In high-speed streaks the minimum of $\overline{v^2 - w^2}$ occurs at the wings of the streak (cf. figure 22) indicating the dominance of the $\mathcal{V}$ fluctuations over the $\mathcal{S}$ at the wings of the streak, as is clear in figure 19 from the contribution to this stress from the $\mathcal{S}$ and $\mathcal{V}$ fluctuations separately.

9. Tracing the origin of the universality of the Reynolds stresses supporting the R-S to the optimal growth of perturbations on the R-S

We have seen that there is a universal mechanism producing Reynolds stresses properly collocated to result in streak growth in turbulent shear flow. This remarkable result has precedence in earlier work in which it was shown that even an infinitesimal streak perturbation imposed on a spanwise homogeneous field of turbulence in a spanwise constant mean shear flow organizes roll-inducing Reynolds stresses resulting in an unstable mode with R-S form arising from the streak perturbation (Farrell & Ioannou 2012; Farrell *et al.* 2017*b*, 2022). This result was ascribed to the structure of optimal perturbations which dominate the perturbation variance as a necessary consequence of the completeness of basis functions which requires that a sufficiently random field will have a projection on every basis function and in a non-normal dynamics, such as a shear flow, only a small set of these projections grow appreciably over time in the energy norm. These structures can be identified using singular value decomposition to be the optimal perturbations. It follows that in the stochastic background field of shear turbulence a small set of optimal perturbations form a basis in the energy norm for the set of energy active fluctuations that determine the fluctuations obtaining significant amplitude. The hypothesis to be tested is whether the optimal perturbations on a streak in a shear flow evolve correlated with the streak just so as to force the streak to grow by inducing roll forcing that results in a streak-amplifying lift-up process. The implication of this hypothesis being verified is that, in the random field of the turbulent background, the set of growing structures that spontaneously develop are responsible for the universality of the Reynolds stresses and also that these optimal perturbations tend to destabilize any perturbation with streak form giving rise to a universal streak destabilizing mechanism that is a general property of turbulence in shear flow.

We test this hypothesis by calculating the ensemble mean covariance of stochastically excited perturbations imposed on a mean streak using a stochastic turbulence model (STM). In this STM the ensemble mean covariance, $\boldsymbol{C}_{k_x}$, of the fluctuations with streamwise wavenumber k_x (cf. (3.2)) that develops with white-in-time and white-in-energy stochastic excitation through the non-normal interaction with the mean flow, U, satisfies the time-dependent Lyapunov equation which can be written in matrix

form as

$$\frac{\mathrm{d}\boldsymbol{C}_{k_x}}{\mathrm{d}t} = \boldsymbol{A}_{k_x}(U)\boldsymbol{C}_{k_x} + \boldsymbol{C}_{k_x}\boldsymbol{A}^{\dagger}_{k_x}(U) + \boldsymbol{I}, \tag{9.1}$$

which, it is useful to note, is also the second cumulant equation of S3T. Here $\boldsymbol{A}_{k_x}(U)$ is the linear operator governing the evolution of the fluctuations with wavenumber k_x about the mean flow, U; $\boldsymbol{I}$ is the spatial covariance of the stochastic forcing, which is taken as the identity in order that all degrees of freedom are excited equally in energy; † denotes the Hermitian transpose (Farrell & Ioannou 1993*b*). The mean flow $U\hat{\boldsymbol{x}}$ considered is hydrodynamically stable (it is our stable low- or high-speed streak). While all fluctuations eventually decay, continual excitation produces a finite covariance, which is dominated by the structures that grow the most by non-normal interaction with the mean flow. These dominantly growing structures are the optimal perturbations. In Nikolaidis *et al.* (2023) the dominant POD modes of the covariance that develops in (9.1) in the background of the time-mean low-speed streak shown in figure 1 were obtained. It was shown there that the dominant POD modes reflect the average structure of the optimal perturbations that grow on the streak and consequently provide a characterization of the Reynolds stresses and of the induced roll forcing.

First consider the covariances that develop when the mean flow U in (9.1) is spanwise independent. This to a good approximation occurs in the upper region, $y/h > 1$, of the time mean flow in figure 1. In that case the $\mathcal{S}$ and $\mathcal{V}$ fluctuation components are identical modulo a spanwise shift, the velocity fields are statistically spanwise homogeneous and the associated Reynolds stresses do not produce roll forcing as $\langle\overline{v^2 - w^2}\rangle$ is spanwise constant and $\langle\overline{vw}\rangle = 0$ (cf. (5.4)). The vanishing of $\langle\overline{vw}\rangle$ can be seen by noting that the $\mathcal{S}$ contribution to this stress is equal and opposite to the $\mathcal{V}$ contribution. As a result, the streak acceleration vanishes in the homogeneous regions $y/h > 1$ above the low-speed streaks, as shown in figures 15*a*, 17*a*. Upon introducing in (9.1) the mean flow of the streak of figure 1, indicated as U_s, the covariances are no longer spanwise homogeneous and the Reynolds stresses produce roll forcing. Consider (9.1) integrated forward with the streak mean flow in figure 1 and initial condition the spanwise homogeneous equilibrium covariance, $\boldsymbol{C}_{hom,k_x}$, that emerges asymptotically when the mean flow is the spanwise independent time-mean flow $U_m(y)$. The inhomogeneous covariance $\boldsymbol{C}_{inh,k_x}$ that develops according to (9.1) in time δt after the introduction of the streak is

$$\boldsymbol{C}_{inh,k_x} = (\delta A_{k_x}(U_s)\boldsymbol{C}_{hom,k_x} + \boldsymbol{C}_{hom,k_x}\delta A^{\dagger}_{k_x}(U_s))\delta t, \tag{9.2}$$

with $\delta A_{k_x}(U_s) = A_{k_x}(U_m + U_s) - A_{k_x}(U_m)$. The Reynolds shear and normal stresses produced by $\boldsymbol{C}_{inh,k_x}$ are shown in figure 23(*a*,*b*) after integration of (9.1) for $\delta t = 0.001h/U_c$ units of time. The roll-circulation induced through the straining of the spanwise homogeneous velocity field over this short interval of time is shown in figure 23(*c*–*f*). Remarkably, the universal structure of the Reynolds stresses and of the roll forcing seen in the time mean statistics of NSE100 and RNL100 manifests instantaneously upon the introduction of the streak in the flow. This indicates that straining over an infinitesimal time interval of a spanwise homogeneous fluctuation field by a low-speed streak favours the $\mathcal{S}$ component of the field over the $\mathcal{V}$ producing correctly configured roll forcing to destabilize the streak.

Note that because $\delta A_{k_x}(U_s)$ depends linearly on U_s, reversing the sign of U_s in (9.2) reverses the sign of all the Reynolds stresses and (9.2) predicts that a high-speed streak strains a spanwise homogeneous field of turbulence to produce push-down reinforcing the high-speed streak. Because changes of the strength of the streak in (9.2) are associated

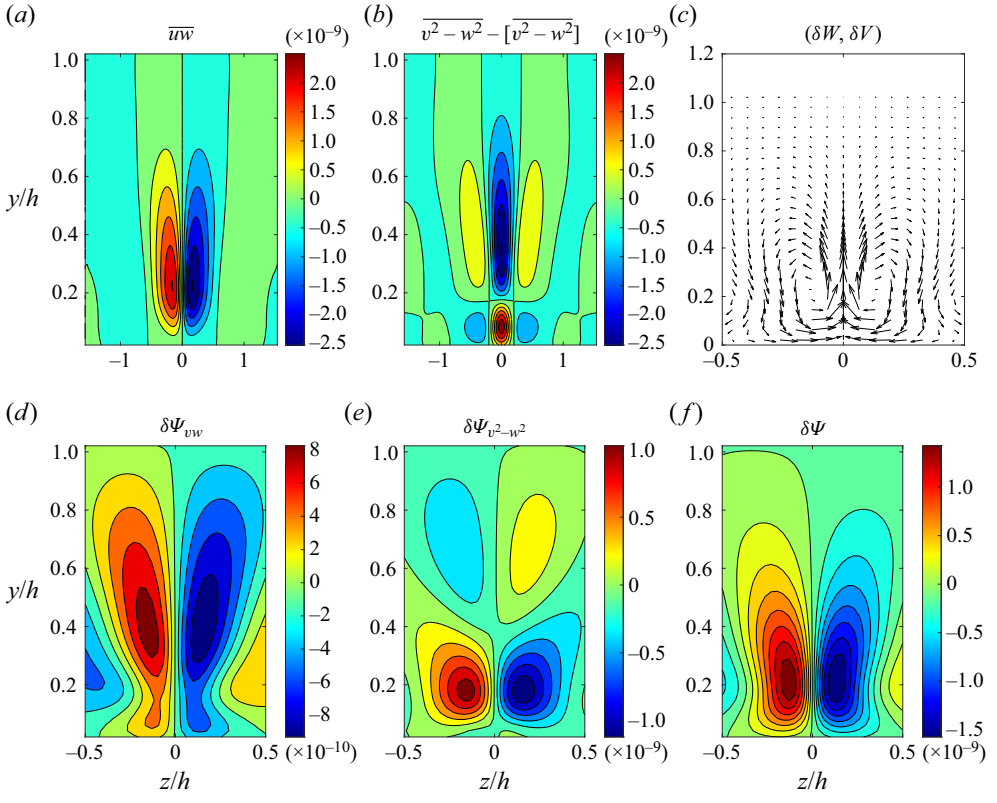

Figure 23. Reynolds stresses predicted by the STM about the NSE100 low-speed streak: the ensemble mean Reynolds shear stress $\langle\overline{vw}\rangle$ (*a*), and the dynamically relevant asymmetric Reynolds normal stress component $\langle\overline{v^2 - w^2}\rangle$ (*b*). Also shown in (*c*) is the roll circulation $(\delta W, \delta V)$ induced in unit time by both components of the Reynold stress. The stream function $\delta\Psi_{vw}$ of the roll circulation induced by $\langle\overline{vw}\rangle$ is shown in (*d*) and the stream function $\delta\Psi_{v^2-w^2}$ of the roll circulation induced by $\langle\overline{v^2 - w^2}\rangle$ is shown in (*e*), while the total stream function $\delta\Psi = \delta\Psi_{vw} + \delta\Psi_{v^2-w^2}$ is shown in (*f*) (the contour interval in (*d*,*e*,*f*) is $2 \times 10^{-10} h U_c$). These Reynolds stresses and roll circulations emerge when a spanwise homogeneous field of fluctuations white-in-energy with $k_x/\alpha = 3$ is strained for only $0.001 h/U_c$ units of time by the low-speed streak of figure 1 centred at $z = 0$. This figure shows that the universal structure of the Reynolds stresses supporting a streak emerges immediately through the straining of a random homogeneous field of perturbations by the streak.

only with changes in the time scale, these results also apply to infinitesimal streaks and it is in fact the mechanism underlying the exponential growth of the R-S which, while clearly manifested in DNS and RNL, has analytic expression as a modal instability only in the infinite ensemble framework of S3T theory (Farrell *et al.* 2017*b*). This example application underscores the fundamental theoretical importance of analysing the dynamics of an infinite ensemble of realizations and the value of convincingly demonstrating the dynamical similarity among DNS, RNL and S3T in order to exploit the power afforded by the analytic structure of S3T to understand NSE turbulence.

Having shown that infinitesimal straining of a spanwise homogeneous field of turbulence by a low- or high-speed streak produces R-S destabilizing Reynolds stresses, we turn next to straining a turbulent field over a time interval typical of fully developed turbulence by considering the Reynolds stresses that develop in the STM (9.1) over a period of $T_d = 30 h/U_c$ initiated with a zero covariance. This period is selected because

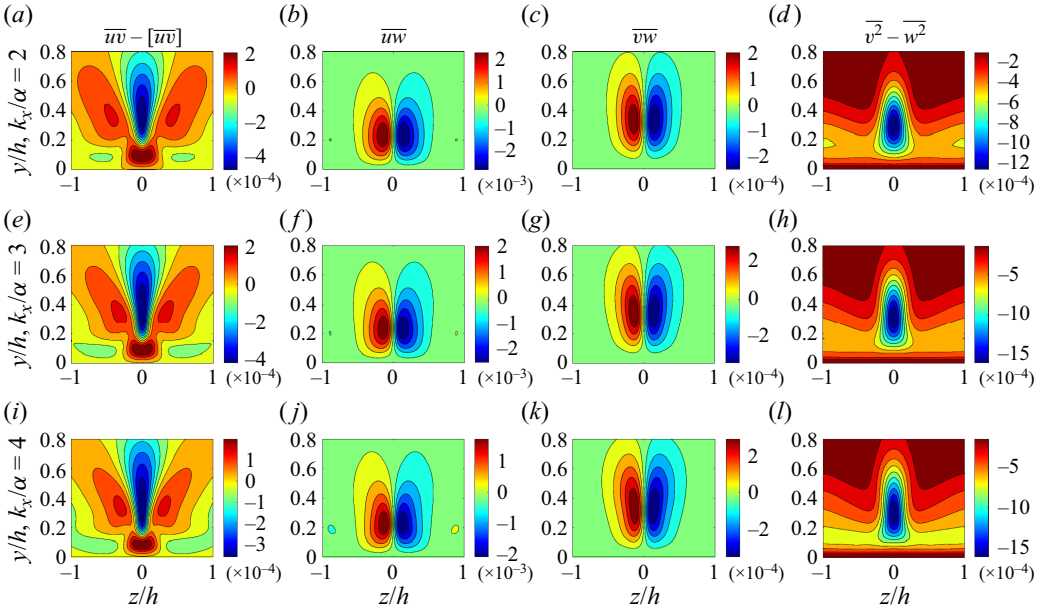

Figure 24. As in figure 20 but showing the time-mean Reynolds stresses of fluctuations obtained using the $T_d = 30h/U_c$ STM covariance resulting from stochastically exciting the time-mean low-speed streak of NSE100 white-in-energy initiated with zero initial covariance. Results are shown for fluctuations with $k_x/\alpha = 2$ (*a–d*), $k_x/\alpha = 3$ (*e–h*) and $k_x/\alpha = 4$ (*i–l*).

it is the typical coherence time of integral scale fluctuations in the turbulent flow (cf. Lozano-Durán *et al.* 2021). The Reynolds stresses that are obtained by the STM with (9.1) are shown in figure 24 (cf. figure 20) for the low-speed streak and figure 25 (cf. figure 22) for the high-speed streak. These Reynolds stresses verify that non-normal linear interaction between the streak and white-in-energy random perturbations give rise to the roll-forcing ensemble mean Reynolds stresses observed in DNS.

Note that in the case of infinitesimal straining the stress distribution in high-speed streaks is identical to that in low-speed streaks with the same structure except for a change in sign (cf. (9.2)). In contrast, the finite time stress distributions in the high- and low-speed streaks of figure 1 differ substantially in structure, as seen in figures 24 and 25. Nevertheless, in both cases the stress distributions induce roll forcing that maintain the imposed streak. The difference in the stress distribution between low- and high-speed finite amplitude streaks results from differences in the optimal perturbation growth in low- and high-speed streaks, which favours the growth of $\mathcal{S}$ optimal perturbations in low-speed streaks, as was previously noted by Hoepffner, Brandt & Henningson (2005).

We illustrate in figure 26 this divergent behaviour of the $\mathcal{S}$ and $\mathcal{V}$ optimals in the presence of the time-mean flows $U_m(y) \pm \varepsilon U_s(y, z)$, where $U_m(y)$ is the spanwise mean flow and $U_s(y, z)$ is the time mean low-speed streak of figure 1 with streak amplitude $\varepsilon = 0, \pm 1$. This figure shows that the optimal perturbation growth increases as the amplitude of the streak increases and that the increase is substantial when the streak is low-speed and marginal when the streak is high-speed. The optimization time $T = 10h/U_c$ was chosen to correspond to the global optimal time. Energy transfer from the mean spanwise shear to the perturbations, $-\int_{\mathcal{D}} \mathrm{d}y\,\mathrm{d}z\overline{uw}U_z$, is the energy source that accounts for the increased perturbation growth in the presence of the streak, and especially so when a

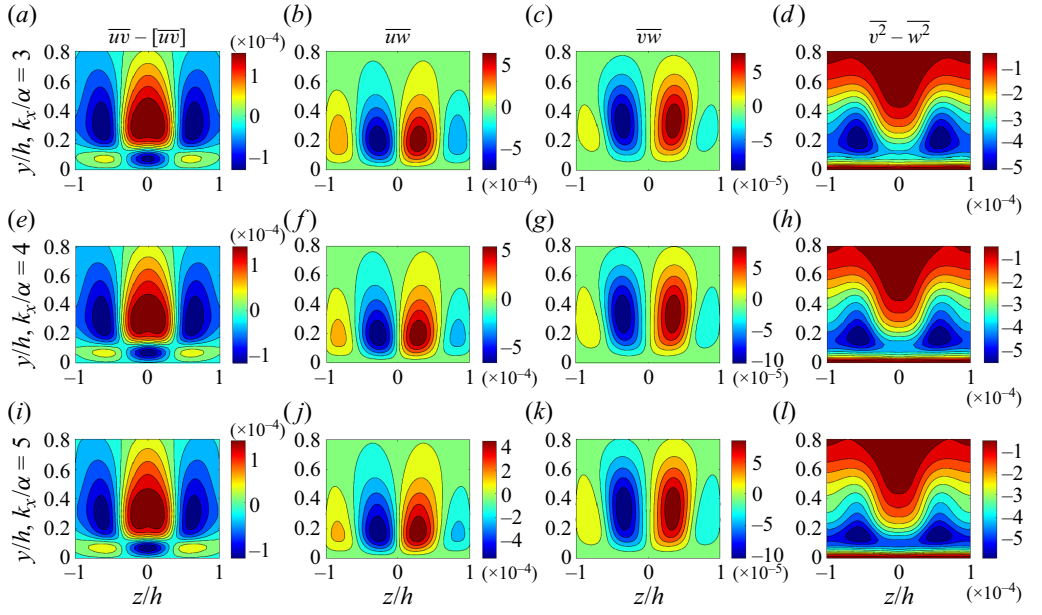

Figure 25. As in figure 22 but showing the time-mean Reynolds stresses of fluctuations obtained using the $T_d = 30h/U_c$ STM covariance resulting from stochastically exciting the high-speed streak of NSE100 white-in-energy initiated with zero initial covariance. Results are shown for fluctuations with $k_x/\alpha = 3$ (*a–d*), $k_x/\alpha = 4$ (*e–h*) and $k_x/\alpha = 5$ (*i–l*).

low-speed streak is present because flows with low-speed streaks have a relatively smaller wall-normal shear and the perturbations are less readily sheared over by the wall-normal shear, which limits their potential growth. Differences in the growth of perturbations in flows of the form $U_m(y) \pm \varepsilon U_s(y, z)$ is expected, because the flows are not mirror images of each other.

The pronounced asymmetry in the growth of optimal perturbations in low-speed and high-speed streaks has dynamical implications. It implies, as we have seen reflected in the time-mean statistics of the DNS and also RNL, that high-speed streaks are supported weakly by their Reynolds stresses, which contributes to the dominance of low-speed streaks in wall-bounded turbulence.

10. Conclusions

In this work we have examined the dynamics supporting the R-S in plane Poiseuille turbulence at $R = 1650$ and verified that this dynamics is substantially the same in RNL and DNS and that it is the mechanism of R-S destabilization by transiently growing structures identified in S3T dynamics (Farrell & Ioannou 2012). Transient growth is shown to destabilize an imposed streak immediately as the background turbulence is strained by the streak and to continue to amplify the streak as optimally growing structures contained in the background turbulence evolve over finite time, as is required for both initial destabilization of the R-S and its maintenance at finite amplitude.

In order to study the R-S formation, maintenance and regulation to its finite amplitude equilibrium we have departed from the traditional decomposition of wall-bounded turbulence into time-mean and fluctuation fields, in which the R-S is relegated to comprise a part of the fluctuation field. We have rather chosen a streamwise-mean decomposition because this partition results in a SSD that comprises the fundamental dynamics of wall

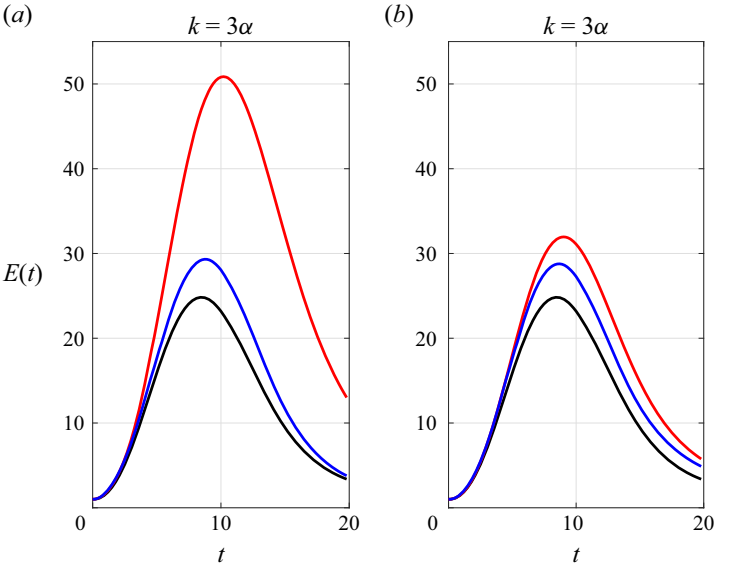

Figure 26. Time evolution of the energy of the $\mathcal{S}$ (red) and $\mathcal{V}$ (blue) $T = 10h/U_c$ optimal perturbations in a flow with a low-speed streak (*a*) and a high-speed streak with the same structure (*b*) for streak amplitude $\varepsilon = 1$. The corresponding energy growth of the $\mathcal{S}$ and $\mathcal{V}$ optimals with no streak $\varepsilon = 0$ are indicated with the black line, in this case the growth of the $\mathcal{S}$ and $\mathcal{V}$ optimal perturbations is equal. This figure shows that the spanwise shear increases the energy growth of both $\mathcal{S}$ and $\mathcal{V}$ perturbations but that the low-speed streak supports substantially greater growth of the $\mathcal{S}$ optimal perturbation. Perturbations have $k_x/\alpha = 3$.

turbulence in a transparent manner. With the R-S contained in the mean flow we obtain a second-order closure, referred to as S3T (Farrell & Ioannou 2012), that concisely captures the structure and dynamics of wall turbulence.

The validity and utility of S3T theory is evident from the fact that it provides the means for the analytic study of the stability of the attractors of the SSD of turbulent shear flows. Consider as example a plane wall-bounded flow with a statistical mean equilibrium profile consistent with an externally supplied spanwise homogeneous field of random fluctuations (a field of free stream turbulence). Application of S3T perturbation stability analysis reveals that this spanwise-uniform mean flow and its associated fluctuation cumulant is modally unstable at large enough Reynolds numbers, giving rise to a mean flow that includes rolls and streaks (Farrell *et al.* 2017*b*). That this fundamental symmetry-breaking instability has analytic expression only in S3T, while being clearly manifest in both DNS and RNL, indicates the analytic utility of adopting S3T for the study of turbulence in shear flow. This point of view is implicitly adopted in the classical picture of the SSP cycle (Hamilton *et al.* 1995), which involves a self-sustaining quasilinear interaction of the streamwise-mean with the fluctuations, as analytically embodied in the S3T/RNL dynamics. Because S3T and RNL have the same dynamical structure (RNL is essentially S3T with the second cumulant approximated by a finite ensemble) we can take RNL simulations as confirming at higher Reynolds numbers than S3T can be integrated that this quasilinear interaction, with this definition of the mean, produces, within the framework of the NSE, a sustained SSP cycle and realistic turbulent states (Thomas *et al.* 2014; Bretheim, Meneveau & Gayme 2015; Farrell *et al.* 2016, 2017*a*). The key ingredient of the SSP cycle, as identified in Farrell & Ioannou (2012) and extensively verified in RNL simulations, is that in the presence of a streak the non-normal growth of fluctuations results in Reynolds

stresses that drive roll circulations that reinforce the pre-existing streaks in the flow. This is also the underlying mechanism of the S3T modal instability discussed in Farrell & Ioannou (2012) and Farrell *et al.* (2017*b*): any flow perturbation with streak form induces ensemble fluctuation Reynolds stresses that lead to collocated roll circulations that, at high enough Reynolds numbers, lead to exponential growth of the R-S. In this work we began by verifying that the turbulent fluctuations in DNS and in RNL become configured in the presence of a streak so as to induce roll circulations that reinforce pre-existing streaks in the flow. While roll forcing by fluctuation Reynolds stresses was previously identified and verified to be the mechanism of R-S formation in S3T, RNL and DNS, the exact dynamical mechanism producing the required collocated roll forcing was left unidentified. In this work we showed using data from a DNS that in the time mean the $\mathcal{S}$ and $\mathcal{V}$ components of the fluctuations are linearly statistically independent and it is the $\mathcal{S}$ fluctuations about the centreline of the streak that produce roll circulations leading to lift-up in shear regions, strengthening pre-existing low-speed streaks and weakening high-speed streaks, while it is the $\mathcal{V}$ fluctuations that produce the opposite effects resulting in amplification of high-speed streaks. In a homogeneous turbulent background field and without a perturbation of streak form these opposing streak-forming tendencies cancel exactly leading to no roll formation. However, in the presence of a streak, exact stress balance between the $\mathcal{S}$ and $\mathcal{V}$ components is disrupted so that for a low-speed streak the $\mathcal{S}$ roll-forming stresses dominate over the $\mathcal{V}$ roll-destroying stresses while the opposite is true in high-speed streaks. In this way the presence of a streak partitions the fluctuation stresses between $\mathcal{S}$ and $\mathcal{V}$ components in just the manner required for its amplification. While both the $\mathcal{S}$ and $\mathcal{V}$ fluctuations are present in both low-speed and high-speed streaks, so that, for example, careful data analysis would reveal $\mathcal{V}$ structures consistent with hairpin vortices coincident with low-speed streaks, we show in this work that these $\mathcal{V}$ structures oppose rather than support the low-speed streak.

When diagnosis of the streamwise varying fluctuation Reynolds stresses is made we find that the Reynolds stress term that dominates in the formation and maintenance of the R-S is $\langle \overline{v^2 - w^2} \rangle$, and primarily the $\langle \overline{w^2} \rangle$ component. The distribution of this component results from asymmetry in the non-normal amplifications of the $\mathcal{S}$ and $\mathcal{V}$ fluctuations, and this asymmetry determines the direction of the roll circulation. In a forthcoming publication we explain how this normal stress distribution determines the direction of the roll forcing (Farrell *et al.* 2022). This remarkable identification of the primary role of the asymmetric Reynolds normal stress in the dynamics of the R-S points to a novel interpretation of the origin of this structure that underlies the maintenance of wall turbulence. The utility of verifying that the same mechanism supports wall turbulence in the three representations of NS dynamics, the S3T SSD closure, the RNL approximation of the S3T SSD closure and DNS, lies in the fact that the S3T is analytically complete in the dynamics of its turbulence whereas the DNS has proven recalcitrant to reveal its fundamental dynamics. The S3T/RNL system being both analytically transparent and numerically tractable provides a powerful tool for understanding the fundamental dynamics of wall turbulence. In addition to its theoretical utility, the quasilinear structure of S3T/RNL promises to allow extension of the powerful methods of linear control to address other problems associated with both understanding and controlling turbulence in shear flow.

Declaration of interests. The authors report no conflict of interest.

Author ORCIDs.
Marios-Andreas Nikolaidis https://orcid.org/0000-0002-0603-2850;
Petros J. Ioannou https://orcid.org/0000-0003-2793-5511;
Brian F. Farrell https://orcid.org/0000-0003-4795-4277.

References

del Álamo, J.C. & Jiménez, J. 2006 Linear energy amplification in turbulent channels. *J. Fluid Mech.* **559**, 205–213.

del Álamo, J.C., Jiménez, J., Zandonade, P. & Moser, R.D. 2006 Self-similar vortex clusters in the turbulent logarithmic region. *J. Fluid Mech.* **561**, 329–358.

Alizard, F., Le Penven, L., Cadiou, A., Di Pierro, B. & Buffat, M. 2021 Restricted optimal paths to transition in a plane Couette flow. *Eur. J. Mech. (*B*/Fluids)* **85**, 261–275.

Avsarkisov, V., Hoyas, S., Oberlack, M. & Garcia-Galache, J.P. 2014 Turbulent plane Couette flow at moderately high Reynolds number. *J. Fluid Mech.* **751**, R1.

Benney, D.J. 1960 A non-linear theory for oscillations in a parallel flow. *J. Fluid Mech.* **10** (02), 209–236.

Brandt, L., Schlatter, P. & Henningson, D.S. 2004 Transition in boundary layers subject to free-stream turbulence. *J. Fluid Mech.* **517**, 167–198.

Bretheim, J.U., Meneveau, C. & Gayme, D.F. 2015 Standard logarithmic mean velocity distribution in a band-limited restricted nonlinear model of turbulent flow in a half-channel. *Phys. Fluids* **27**, 011702.

Butler, K.M. & Farrell, B.F. 1992 Three-dimensional optimal perturbations in viscous shear flows. *Phys. Fluids* **4**, 1637–1650.

Cantwell, B.J. 1981 Organized motion in turbulent flow. *Annu. Rev. Fluid Mech.* **13**, 457–515.

Constantinou, N.C., Farrell, B.F. & Ioannou, P.J. 2014 Emergence and equilibration of jets in beta-plane turbulence: applications of stochastic structural stability theory. *J. Atmos. Sci.* **71** (5), 1818–1842.

Cossu, C. & Hwang, Y. 2017 Self-sustaining processes at all scales in wall-bounded turbulent shear flows. *Phil. Trans. R. Soc.* A **375**, 20160088.

Deguchi, K. & Hall, P. 2016 On the instability of vortex-wave interaction states. *J. Fluid Mech.* **802**, 634–666.

Ellingsen, T. & Palm, E. 1975 Stability of linear flow. *Phys. Fluids* **18**, 487–488.

Farrell, B.F., Gayme, D.F. & Ioannou, P.J. 2017*a* A statistical state dynamics approach to wall-turbulence. *Phil. Trans. R. Soc.* A **375** (2089), 20160081.

Farrell, B.F. & Ioannou, P.J. 1993*a* Perturbation growth in shear flow exhibits universality. *Phys. Fluids* A **5**, 2298–2300.

Farrell, B.F. & Ioannou, P.J. 1993*b* Stochastic forcing of the linearized Navier–Stokes equations. *Phys. Fluids* A **5**, 2600–2609.

Farrell, B.F. & Ioannou, P.J. 2012 Dynamics of streamwise rolls and streaks in turbulent wall-bounded shear flow. *J. Fluid Mech.* **708**, 149–196.

Farrell, B.F., Ioannou, P.J., Jiménez, J., Constantinou, N.C., Lozano-Durán, A. & Nikolaidis, M.-A. 2016 A statistical state dynamics-based study of the structure and mechanism of large-scale motions in plane Poiseuille flow. *J. Fluid Mech.* **809**, 290–315.

Farrell, B.F., Ioannou, P.J. & Nikolaidis, M.-A. 2017*b* Instability of the roll–streak structure induced by background turbulence in pre-transitional Couette flow. *Phys. Rev. Fluids* **2** (3), 034607.

Farrell, B.F., Ioannou, P.J. & Nikolaidis, M.-A. 2022 Mechanism of roll-streak structure formation and maintenance in turbulent shear flow. arXiv:2205.07469.

Flores, O. & Jiménez, J. 2010 Hierarchy of minimal flow units in the logarithmic layer. *Phys. Fluids* **22**, 071704.

Froehlich, S. & Cvitanović, P. 2012 Reduction of continuous symmetries of chaotic flows by the method of slices. *Commun. Nonlinear Sci. Numer. Simul.* **17** (5), 2074–2084, special Issue: Mathematical Structure of Fluids and Plasmas.

Halcrow, J., Gibson, J.F., Cvitanovic, P. & Viswanath, D. 2009 Heteroclinic connections in plane Couette flow. *J. Fluid Mech.* **621**, 365–376.

Hall, P. & Sherwin, S. 2010 Streamwise vortices in shear flows: harbingers of transition and the skeleton of coherent structures. *J. Fluid Mech.* **661**, 178–205.

Hall, P. & Smith, F. 1991 On strongly nonlinear vortex/wave interactions in boundary-layer transition. *J. Fluid Mech.* **227**, 641–666.

Hamilton, J.M., Kim, J. & Waleffe, F. 1995 Regeneration mechanisms of near-wall turbulence structures. *J. Fluid Mech.* **287**, 317–348.

Hellström, L.H.O., Marusic, I. & Smits, A.J. 2016 Self-similarity of the large-scale motions in turbulent pipe flow. *J. Fluid Mech.* **792**, R1.

Hellström, L.H.O., Sinha, A. & Smits, A.J. 2011 Visualizing the very-large-scale motions in turbulent pipe flow. *Phys. Fluids* **23**, 011703.

Hoepffner, J., Brandt, L. & Henningson, D. 2005 Transient growth on boundary layer streaks. *J. Fluid Mech.* **537**, 91–100.

Holford, J.J. & Hwang, Y. 2023 A data-driven quasi-linear approximation for turbulent channel flow. arXiv:2305.15043.

HUTCHINS, N. & MARUSIC, I. 2007 Evidence of very long meandering features in the logarithmic region of turbulent boundary layers. *J. Fluid Mech.* **579**, 1–28.
HWANG, Y. 2015 Statistical structure of self-sustaining attached eddies in turbulent channel flow. *J. Fluid Mech.* **767**, 254–289.
HWANG, Y. & COSSU, C. 2010 Self-sustained process at large scales in turbulent channel flow. *Phys. Rev. Lett.* **105**, 044505.
HWANG, Y. & COSSU, C. 2011 Self-sustained processes in the logarithmic layer of turbulent channel flows. *Phys. Fluids* **23**, 061702.
HWANG, Y. & ECKHARDT, B. 2020 Attached eddy model revisited using a minimal quasi-linear approximation. *J. Fluid Mech.* **894**, A23.
JANG, P.S., BENNEY, D.J. & GRAN, R.L. 1986 On the origin of streamwise vortices in a turbulent boundary layer. *J. Fluid Mech.* **169**, 109–123.
JIMÉNEZ, J. 2018 Coherent structures in wall-bounded turbulence. *J. Fluid Mech.* **842**, P1.
JIMÉNEZ, J. & MOIN, P. 1991 The minimal flow unit in near-wall turbulence. *J. Fluid Mech.* **225**, 213–240.
JIMÉNEZ, J. & PINELLI, A. 1999 The autonomous cycle of near-wall turbulence. *J. Fluid Mech.* **389**, 335–359.
KIM, J., MOIN, P. & MOSER, R. 1987 Turbulence statistics in fully developed channel flow at low Reynolds number. *J. Fluid Mech.* **177**, 133–166.
KREILOS, T., ZAMMERT, S. & ECKHARDT, B. 2014 Comoving frames and symmetry-related motions in parallel shear flows. *J. Fluid Mech.* **751**, 685–697.
KWON, Y. & JIMÉNEZ, J. 2021 An isolated logarithmic layer. *J. Fluid Mech.* **916**, A35.
LANDAHL, M.T. 1980 A note on an algebraic instability of inviscid parallel shear flows. *J. Fluid Mech.* **98**, 243–251.
LEE, M. & MOSER, R.D. 2018 Extreme-scale motions in turbulent plane couette flows. *J. Fluid Mech.* **842**, 128–145.
LOZANO-DURÁN, A., CONSTANTINOU, N.C., NIKOLAIDIS, M.-A. & KARP, M. 2021 Cause-and-effect of linear mechanisms sustaining wall turbulence. *J. Fluid Mech.* **914**, A8.
LOZANO-DURÁN, A. & JIMÉNEZ, J. 2014 Time-resolved evolution of coherent structures in turbulent channels: characterization of eddies and cascades. *J. Fluid Mech.* **759**, 432–471.
LUMLEY, J.L. 1967 The structure of inhomogeneous turbulence. In *Atmospheric Turbulence and Radio Wave Propagation* (ed. A.M. Yaglom & V.I. Tatarskii), pp. 166–178. Nauka.
MARENSI, E., YALNIZ, G., HOF, B. & BUDANUR, N.B. 2023 Symmetry-reduced dynamic mode decomposition of near-wall turbulence. *J. Fluid Mech.* **954**, A10.
MCKEON, B.J. 2017 The engine behind (wall) turbulence: perspectives on scale interactions. *J. Fluid Mech.* **817**, P1.
MCKEON, B.J. 2019 Self-similar hierarchies and attached eddies. *Phys. Rev. Fluids* **4**, 082601.
MCKEON, B.J. & SHARMA, A.S. 2010 A critical-layer framework for turbulent pipe flow. *J. Fluid Mech.* **658**, 336–382.
MOARREF, R., SHARMA, A.S., TROPP, J.A. & MCKEON, B.J. 2013 Model-based scaling of the streamwise energy density in high-Reynolds-number turbulent channels. *J. Fluid Mech.* **734**, 275–316.
NIKOLAIDIS, M.-A. & IOANNOU, P.J. 2022 Synchronization of low Reynolds number plane Couette turbulence. *J. Fluid Mech.* **933**, A5.
NIKOLAIDIS, M.-A., IOANNOU, P.J., FARRELL, B.F. & LOZANO-DURÁN, A. 2023 POD-based study of turbulent plane Poiseuille flow: comparing structure and dynamics between quasi-linear simulations and DNS. *J. Fluid Mech.* **962**, A16.
PIROZZOLI, S., BERNARDINI, M. & ORLANDI, P. 2014 Turbulence statistics in Couette flow at high Reynolds number. *J. Fluid Mech.* **758**, 327–343.
RAWAT, S., COSSU, C., HWANG, Y. & RINCON, F. 2015 On the self-sustained nature of large-scale motions in turbulent Couette flow. *J. Fluid Mech.* **782**, 515–540.
REDDY, S.C. & HENNINGSON, D.S. 1993 Energy growth in viscous channel flows. *J. Fluid Mech.* **252**, 209–238.
ROBINSON, W.A. 1991 The dynamics of the zonal index in a simple model of the atmosphere. *Tellus* **43** (5), 295–305.
ROWLEY, C.W. & MARSDEN, J.E. 2000 Reconstruction equations and the Karhunen-Loève expansion for systems with symmetry. *Phys.* D **142**, 1–19.
SAXTON-FOX, T., LOZANO-DURÁN, A. & MCKEON, B.J. 2022 Amplitude and wall-normal distance variation of small scales in turbulent boundary layers. *Phys. Rev. Fluids* **7**, 014606.
SCHMIDT, O.T. & SCHMID, P.J. 2019 A conditional space–time POD formalism for intermittent and rare events: example of acoustic bursts in turbulent jets. *J. Fluid Mech.* **867**, R2.
SCHOPPA, W. & HUSSAIN, F. 2002 Coherent structure generation in near-wall turbulence. *J. Fluid Mech.* **453**, 57–108.

TAYLOR, G.I. 1935 Statistical theory of turbulence. *Proc. R. Soc. Lond.* A **151**, 421–478.
THOMAS, V., FARRELL, B.F., IOANNOU, P.J. & GAYME, D.F. 2015 A minimal model of self-sustaining turbulence. *Phys. Fluids* **27**, 105104.
THOMAS, V., LIEU, B.K., JOVANOVIĆ, M.R., FARRELL, B.F., IOANNOU, P.J. & GAYME, D.F. 2014 Self-sustaining turbulence in a restricted nonlinear model of plane Couette flow. *Phys. Fluids* **26**, 105112.
VADAREVU, S.B., SYMON, S., ILLINGWORTH, S.J. & MARUSIC, I. 2019 Coherent structures in the linearized impulse response of turbulent channel flow. *J. Fluid Mech.* **863**, 1190–1203.
WALEFFE, F. 1997 On a self-sustaining process in shear flows. *Phys. Fluids* **9**, 883–900.
WALEFFE, F. 2001 Exact coherent structures in channel flow. *J. Fluid Mech.* **435**, 93–102.
WESTIN, K.J.A., BOIKO, A.V., KLINGMANN, B.G.B., KOZLOV, V.V. & ALFREDSSON, P.H. 1994 Experiments in a boundary layer subjected to free stream turbulence. Part 1. Boundary layer structure and receptivity. *J. Fluid Mech.* **281**, 193–218.
WILLIS, A.P., CVITANOVIĆ, P. & AVILA, M. 2013 Revealing the state space of turbulent pipe flow by symmetry reduction. *J. Fluid Mech.* **721**, 514–540.